Studies on the Module Structure for the NOvA Liquid Scintillator Neutrino Detector

A THESIS

SUBMITTED TO THE FACULTY OF THE GRADUATE SCHOOL

OF THE UNIVERSITY OF MINNESOTA

BY

Michael James Slotman

IN PARTIAL FULFILLMENT OF THE REQUIREMENTS

FOR THE DEGREE OF

MASTER OF SCIENCE

Professor Thomas Chase

December, 2014

Acknowledgements

There are many people who had a part in making this thesis a reality and to whom I am very grateful. First, I would like to thank my adviser, Prof. Thomas Chase for his direction, encouragement, and patience. Thanks to my committee members, Prof. Dan Cronin-Hennessey for envisioning and designing the interaction test and explaining physics, and Prof. Sue Mantell for her generosity in providing lab space and testing equipment.

Many members of the NOνA collaboration and physics department were exceedingly helpful. Jarek Nowak, John Kwong, Zeb Krahn, Kregg Arms, Alex Smith, Minerba Betancourt, Adam Schreckenberger, and Jan Zirnstein were all very helpful and accommodating as well. Thanks to Ken Heller and the NOνA project for providing assistantship support. Nathaniel Pearson and Dick Wildberger providing excellent support at the NOνA module factory, as did many undergrads. Notably, Jake Bobula prepared the majority of the samples for the adhesive aging tests.

Lastly and most especially, I thank my family and friends for providing invaluable encouragement and support throughout my time at the U. My parents, Howard and Diane, offered me unwavering love, constant encouragement, and useful goading. In addition, many thanks to my dad for proofreading numerous drafts. Friends from Hope Community Church, small groups, and Bethel have been important supporters and encouraged me greatly. You are all awesome, and I'm grateful you are a part of my life.

Dedication

To my parents, Howard and Diane, I dedicate this thesis, which, without their love, support, and encouragement, would not exist.

Abstract

This thesis contains studies pertinent to the construction of modules for the NOνA experiment detectors.

The tensile strength of acrylic and epoxy adhesives used in construction of the detector was studied over time and with various surface preparations. Sanding and corona discharge surface treatments increased the bond strength of the acrylic by 10-20%; aging in oil did not affect the acrylic bond strength while aging in air at 50°C for 9 months (equivalent to approximately 5 years at room temperature) increased the acrylic bond strength by 25%. For the epoxy, corona discharge treated samples' strength increased slightly after aging while the strength of sanded samples in air remained consistent and sanded samples in oil decreased by 17% when aged at 50°C for 1.5 years (equivalent to approximately 10 years at room temperature).

All materials used in the detector were studied to determine if degrading interaction would occur with the pseudocumene liquid scintillator. Substances such as acrylic adhesive and PTFE paste were found to interact with the scintillator while materials such as a variety of PVCs, epoxy adhesives, and PTFE tape were found to be non-reactive with the scintillator.

Following the appearance of cracks on manifold covers in installed modules, studies were carried out to help to determine the cause and mitigation of these cracks. Manifold covers that had been pressure tested at various pressures during the check of the seals during the manufacturing process were examined for the formation of cracks. "Containment units" were used to constrain the swelling of the manifold covers during pressure testing. Internal cracks were visible on the majority of manifold covers tested at 1.4 bar with the original containment units. It was found that reducing the pressure testing

of the modules from 1.4 bar to 0.7 bar and increasing the rigidity of the pressure test containment units eliminated the formation of visible cracks in the manifold covers.

Stress concentration in small fillet radius injection molded PVC was studied. Geon M3500 PVC has a yield strength 12% greater than Geon M3800 PVC originally used for the manifold covers but increased the stress concentrated failure time by 6600% and was thus chosen to mold new manifold covers after a redesign to eliminate stress concentrating features.

Contents

List of Tables

List of Figures

Chapter 1

Introduction to the NOνA Experiment and the Studies Contained in this Thesis

The NOνA detectors are mainly constructed from extruded and injection molded PVC and fastened together with various adhesives. This thesis describes a series of studies examining the strength trends for various adhesives used in detector construction, compatibility of all detector construction materials with the scintillator chemicals used in the detector, and various aspects of injection molded PVC cracking which occurred in the manifold cover.

In this introductory chapter, Section 1.1 describes the research goals of the NOνA project. Section 1.2 describes the various components of the detector modules and how the modules fit together. Finally, Section 1.3 describes the purpose of the studies in the following chapters and how they relate to the detector and the NOνA project.

1.1 Introduction to the NOνA Experiment

The NOνA experiment has three stated objectives. The first objective is to observe the oscillation of muon neutrinos into electron neutrinos. The second objective is to determine the ordering of neutrino mass. The third objective is to find if there is a symmetry between neutrinos and antineutrinos.[1]

1.1.1 Oscillation of Muon to Electron Neutrinos

There are three flavors of neutrinos, muon, electron, and tau. Neutrinos oscillate from one flavor to another as they travel. Although oscillations of other flavors have been observed, the oscillation from muon to electron neutrinos has not yet been observed.

The NOνA experiment is designed to see if it is possible to observe the oscillation of muon neutrinos into electron neutrinos and likewise muon antineutrinos into electron antineutrinos. The answer to this question will help provide a better understanding of neutrino behavior.[2]

1.1.2 Ordering of Neutrino Mass

Another goal of the NOνA experiment is to determine the ordering of the neutrino mass. There are three flavor combinations of neutrinos resulting in neutrinos with different masses. By comparing the neutrino beam to the antineutrino beam, it will be determined if a certain neutrino type is the heaviest or the lightest.[3]

1.1.3 Symmetry between Neutrinos and Antineutrinos

Finally, the NOνA experiment will study the symmetry between matter and antimatter by observing if antineutrinos oscillate at the same rate as neutrinos. If this is not the case, there may not be symmetry between matter and antimatter which could explain

why more matter exists in the universe than antimatter. A difference between the oscillations of neutrinos and antineutrinos could indicate a violation of charge-parity symmetry.[1]

1.2 The NOνA Experiment Components and Detectors

NOνA is an acronym for the NuMI Off-Axis ν_e Appearance experiment. The experiment uses the NuMI neutrino beam generated at Fermilab. The NOνA detectors are located slightly off-axis from the NuMI beam to optimize the flux of neutrinos at the desired energy. This energy will give the detector the best chance to observe the oscillation of muon neutrinos into electron neutrinos.

The NOνA experiment is composed of two liquid scintillator detectors and makes use of the NuMI neutrino beam generated at Fermilab. The Near Detector is located underground at Fermilab while the the Far Detector is located at surface level in Ash River, Minnesota. A third, smaller detector, called the Integrated Prototype Near Detector or IPND, is located at Fermilab at surface level and used as a prototype for the Far Detector and collects data from the NuMI beam and from cosmic radiation.

The NuMI neutrino beam is generated from the Fermilab particle accelerator. It can produce a 700 kW beam of muon neutrinos or antineutrinos. A proton beam is focused on a target which generates pions which then decay into muons and muon neutrinos. The NuMI beam is pointed downward at 3.3 degree angle and emerges in northern Minnesota. The beam travels 810 km reaching a depth of 10 km underneath Wisconsin. In northern Minnesota at the far detector location, the beam is several miles wide and the Far detector is positioned 14 mrad off-axis.

The Near Detector is located beneath Fermilab at the end of the NuMI beam tunnel. The near detector is about 3 meters by 5 meters by 10 meters with a mass of 330 metric tons. As it has such a large flux of neutrinos passing through it, it does not need to be

nearly as large as the Far Detector.

The far detector has a mass of 14 metric kilotons and dimensions of 16 m by 16 m by 67 m. It is located in northern Minnesota in Ash River. The far detector is constructed in a large hole excavated in the surface of a bluff. Because the detector has three dimensional resolution and a narrow trigger window for neutrino interaction, the detector can filter out only neutrino interactions from the NuMI beam and thus did not need to be constructed deep underground like the MINOS experiment[4] in the Soudan Mine.

The detector is made up of sections of extruded PVC cells filled with liquid scintillator and wavelength-shifting optical fibers.

Alternating layers of vertical and horizontal modules allow three dimensional resolution in the detector. Each module is made up of two PVC extrusions of sixteen long cells. Each cell is 56 by 36 mm, and each extrusion is 66 mm by 635 mm by 15.5 m.

Each cell contains a loop of optical fiber. The fiber ends exit the top of the module where they are directed to an avalanche photo diode (APD) to read the signals (see Fig. 1.1).

An end cap covers one end of the module. Side seals and center seals fit the end cap to the contours of the extrusions to prevent leaking and ensure joint strength. The geometry of the end cap and seals can be seen in Fig. 1.2.

On the other end of the module, the manifold end, the detector signals are read out. The optical fiber ends from each cell are gathered and directed to one side with injection molded PVC grooved parts called raceways which hold each fiber in place. The fibers are glued into an optical connector with each pair of fiber ends grouped together. An exploded view of the manifold end can be seen in Fig. 1.3.

The manifold cover and snout are injection molded PVC parts which provide a covering for the raceways and fibers. The APD reads out the light signals from optical

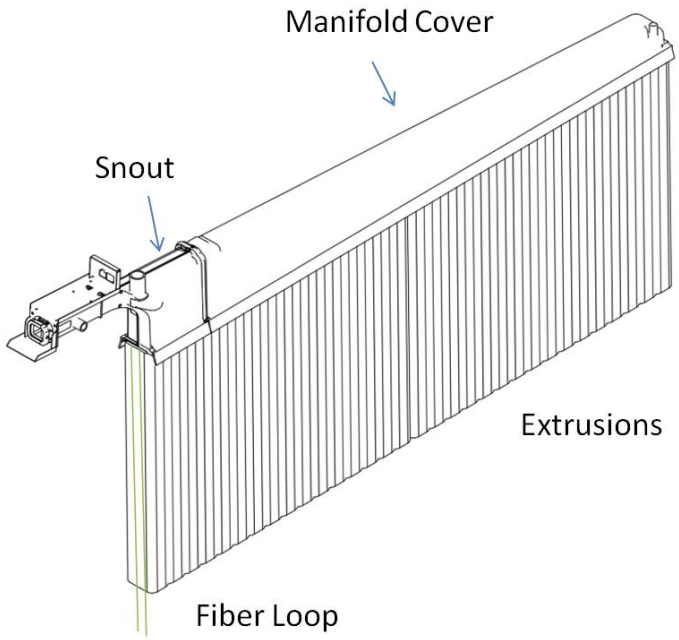

Figure 1.1: The manifold end of a Far Detector module.

fibers with both ends of each loop being read as one pixel. The requisite electronics to operate the APD are also included in an electronics box on each module.

Two part adhesive joints are used for the structural joints between PVC parts. The outer seal uses an acrylic adhesive which gives the joint most of its strength but degrades the liquid scintillator if allowed to be in contact with it. The second inner seal uses an epoxy adhesive which does not add as much strength to the joint but does act to protect the scintillator oil from the acrylic adhesive.

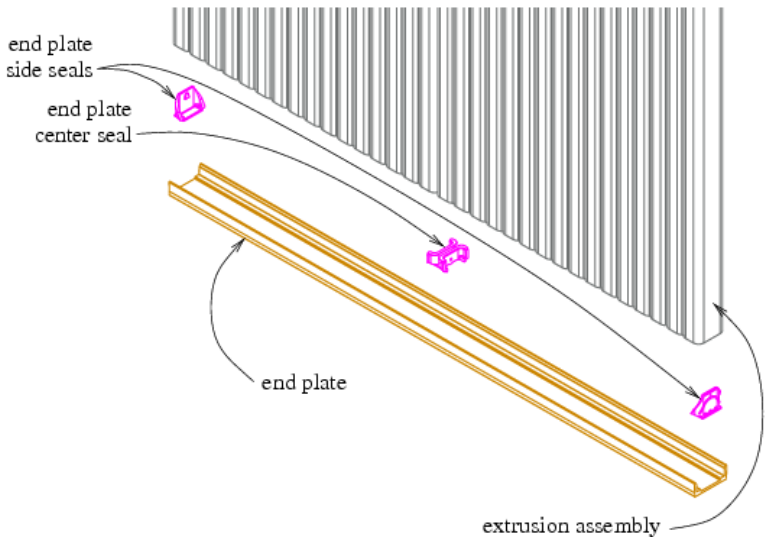

Figure 1.2: An exploded view of the end cap with side and center seals.[5]

1.3 The Studies Contained in This Thesis

This thesis contains several studies performed to test and explore various aspects of the detector's construction. Chapter 2 contains studies on adhesives used in the detector, looking at the strength as aged and the strength after various surface treatments. Chapter 3 describes a study of the interaction of the detector's liquid scintillator with materials used to construct the detector to ensure no material in contact with the scintillator will cause loss of efficacy. Chapter 4 contains several studies investigating the strength and behavior of the injection molded PVC manifold cover, which exhibited cracking in some modules in the IPND.

1.3.1 Adhesive Strength Experiments

The NOνA detectors are mainly constructed from PVC and adhesive. Since the experiment is scheduled to take data for at least ten years, studying the strength of the

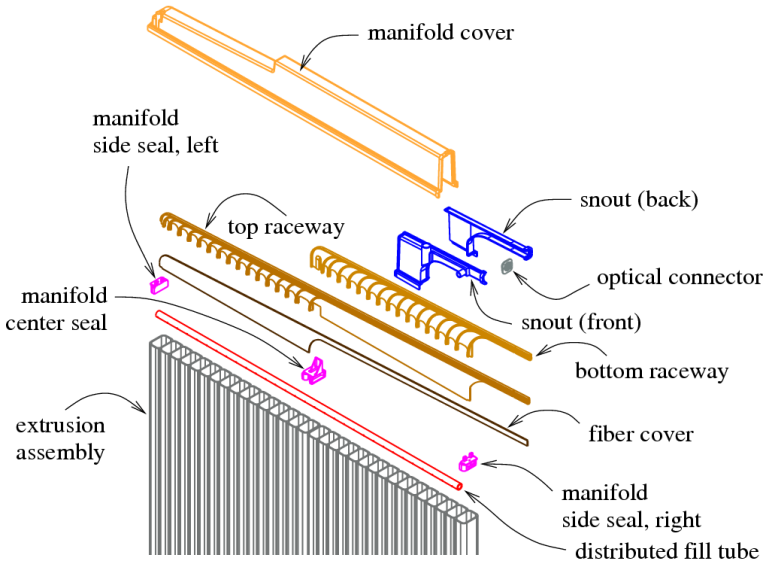

Figure 1.3: An exploded view of the manifold end of a NOνA module.[5]

adhesive-PVC bond as it ages is important. Chapter 2 describes these studies of adhesive strength.

Two main adhesive types were studied, an acrylic which provided the primary structural strength to the dual-adhesive bond, and an epoxy which protected the scintillator from contacting the acrylic and also provided additional strength. Samples of both adhesive types were aged in a hot box to accelerate the aging process and compared to un-aged samples. Some samples in the hot box were submerged in mineral oil to simulate the seals in the detector in contact with the scintillator oil.

Surface treatment of the PVC substrate can impact the strength of the adhesive bond. For both the acrylic and epoxy adhesives, the PVC surfaces were treated by either sanding the PVC surface or by treating the surface with corona arc discharge.

The results and discussion of the acrylic and epoxy strengths are provided in Sections 2.3.1 and 2.3.2, respectively.

1.3.2 Scintillator Interaction

The liquid scintillator is an essential and large part of the detector. The active scintillating compound, pseudocumene, can degrade if exposed to certain materials or chemicals. All potential materials for use in construction of the detector that would contact the scintillator were tested for interaction with the scintillator.

Any material found to interact with the scintillator was either isolated from the scintillator or the material was rejected and another non-interacting replacement found. For example, the acrylic adhesive used as the primary structural adhesive in the construction of the modules was found to degrade the scintillator, so dual-adhesive seals were used with an inner seal of an epoxy adhesive found to have no interaction with the scintillator. Additionally, a PTFE paste was found to interact strongly with the scintillator so the paste was discarded and a PTFE tape which had no interaction was used instead as discussed in Section 3.5.

1.3.3 Injection Molded PVC Strength and Behavior Studies

After modules were assembled into blocks for the IPND, cracks were found to form through the manifold cover in several modules. These cracks all formed at the third rib of the manifold cover where an ejector pin rib was reinforced by a webbing designed to hold the fiber raceway in place as seen in Fig 4.1.

In the module assembly process, after the manifold covers and the other parts are glued together, each module is pressurized to ensure that there are no leaks in any of the adhesive seals and that the module seals will be able to withstand the pressure of the scintillator oil column once filled and will not leak. During this pressure test, the manifold cover is supported with an aluminum containment unit to inhibit it from bending.

The studies in Chapter 4 were performed to learn more about the injection molded

PVC used to produce the manifold covers and learn more about the nature of the cracks and how to mitigate future cracking in the IPND and Far Detector.

The first study, described in Section 4.1, examined the tensile strength of the injection molded PVC in various locations on the manifold cover. These locations included several across Rib 3 and vertically and horizontally along the front, back, and top of the manifold cover as can be seen in Fig. 1.4. Comparisons were made between the strength of the manifold cover PVC parallel to the injection molding grain of the PVC versus perpendicular to the grain.

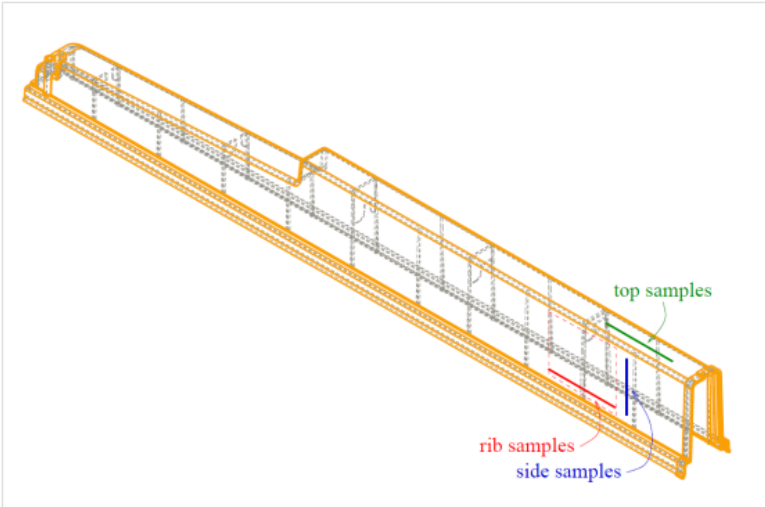

Figure 1.4: The locations on the manifold cover from which the tensile strength test samples were taken.

The second study, described in Section 4.2, looked at stress concentration at small fillet radius corners in the variety of injection molded PVC used in the manifold covers. The snout backs are made from this same PVC as the manifold covers and were used in this test. The bending strength of an L-shaped portion of the snout back with a small fillet radius was observed for two varieties of PVC and for two fillet radii. Longer term

observations were made for samples at various stress levels.

The third study, described in Section 4.3, looked for crack initiation in manifold covers that had been pressure tested at various pressures with two different containment units. While only observed on the inside surface of the manifold cover, these small cracks could potentially grow until they cracked all the way through the manifold covers. It was found that reducing the pressure and using stiffer containment units during the pressure tests eliminated the observed cracks on the manifold cover.

Chapter 2

Adhesive Strength Studies for NOνA Module Construction

The NOνA project is designed to gather data for at least ten years. The NOνA detectors are constructed from extruded and injection molded PVC fastened together with various adhesives. The strength of the adhesive bond can change over time and with exposure to various chemicals. As the detector must remain operational for ten years, the adhesive bonds must not fail as they age in the final detector assembly. Therefore, in this chapter, the performance of the adhesives over time is examined.

It was decided to use a dual-adhesive seal to build the detector modules as shown in Fig. 2.1. Acrylic adhesive adds structural strength to the adhesive joints. Because the acrylic adhesive would quickly degrade the scintillator oil in the detector, as described in Section 3.5.1, an epoxy was used as a barrier to prevent the scintillator from coming into contact with the acrylic. The performance of both the acrylic and the epoxy over time is essential as a failure of either adhesive could cause the project to be fail.

Additionally, it was desired to determine what surface treatment should be applied to the PVC to maximize the strength of the adhesive bonds. Treating the surface with

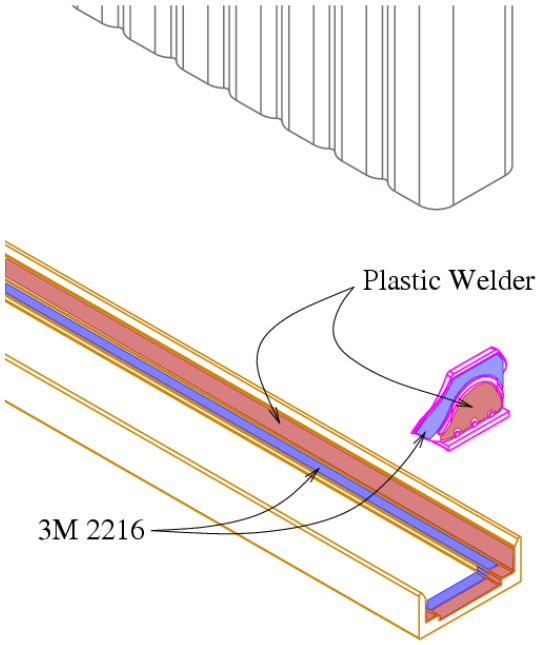

Figure 2.1: The dual-adhesive seal with an acrylic (Plastic Welder) providing structural strength and an epoxy (3M 2216) ensuring the acrylic does not contact the scintillator.[5]

corona discharge and with sanding were compared to untreated PVC.

Section 2.1 of this chapter describes the variables tested in this experiment as well as the apparatuses used in the experiment. Section 2.2 details sample preparation for tests of variables including PVC surface treatment and aging of samples in a hot box. Section 2.3 reports the results of the strength tests for the various variables and discusses the implications for the NOνA project.

2.1 Adhesive Strength Studies Setup

Two primary variables were tested in this experiment. The first was the strength of the adhesive over time as it aged in a hot box. The second variable examined was the

effect of treating the surface of the PVC before adhesive application with either corona discharge or sanding.

The strength versus time study employed a hot box to accelerate the aging of the adhesive samples. The study examined several aspects of adhesive aging including aging in scintillator oil or in air and treatment of the plastic surfaces bonded by the adhesive.

The final group of samples examined how various treatments of the PVC surface affects adhesive strength. Methods for increasing the glue strength, including sanding and corona arc discharge, were examined.

2.1.1 Adhesive Strength Versus Time Setup

Because of the timescale of the detector, it is important know how the adhesive will behave over a long period of time. Three batches of samples were prepared for nine month increments of aging in the hot box, yielding final times of eighteen, nine, and zero months.

Some adhesive will be in contact with the scintillator oil while in the detector. To observe how ten years of exposure to oil will affect the adhesive strength, a duplicate set of each sample type and surface treatment was aged in detector-strength scintillator oil at the increased temperature. By comparing to samples aged in air, the impact of aging in oil can be seen.

The oldest batch was aged in the hot box for eighteen months. This batch consisted of epoxy samples of tensile, shear, and cleavage-peel stress loading sample types. The samples were all surface treated by sanding. Some samples were aged immersed in scintillator oil while the remainder were aged in air.

As the corona discharge machine used for module production had not yet been obtained, only sanded specimens were included in these sample sets. In addition, acrylic samples were not included in the eighteen month sets.

The second batch was aged for nine months in the hot box. This batch included both epoxy and acrylic samples. Both adhesive types had samples of all three test types. Sample sets of both adhesive types were prepared with corona discharge and sanding surface treatment. One complete set of each surface treatment for each adhesive type was aged in scintillator oil while a second complete set was aged in air.

The final batch of samples were freshly created and not aged in the hotbox to give zero time baseline strength. The samples were cured in accordance with the times specified in Section 2.2.2 to ensure a complete cure. In this batch, both epoxy and acrylic samples were prepared with both corona discharge and sanding surface treatment.

Hot Box Aging Details

Given the time limitations associated with the project, the aging process of the adhesive needed to be accelerated to gain insight into long term strength. To achieve this, the samples were aged at a high temperature. A plywood box with 1 inch Styrofoam sheet insulation was constructed with a heater and a fan inside. A thermostat controlling the heater and fan operation was set to keep the box at a constant 50°C. Since this temperature is still well under the glass transition temperature of a typical rigid PVC of around 80°C[6] and the testing will be done at room temperature, the high temperature of the aging should not affect the strength of the PVC.

Our tests are based on a guideline[1] that aging effects are approximately accelerated by a factor of 2 for each 10°C increase in temperature. Assuming a room temperature of 23°C, the equivalent aging time is equal to the following:

$$t_2 = t_1 2^{\frac{50-23}{10}} = t_1 2^{2.7} = 6.5 t_1 \tag{2.1}$$

[1] This guideline was suggested by a vendor. We have not yet been able to validate it in the literature. The guideline could be related to the general guideline that chemical reactions are approximately accelerated by a factor of 2 for each 10°C increase in temperature.

Samples were aged in the hot box for a length of 1.5 and 0.75 years. This is approximately equivalent to an accelerated time of about ten and five years, respectively. Thus this accelerated aging can provide insight into adhesive strength on a time length on the order of the lifespan of the detector.

2.1.2 Surface Treatment Experiments Setup

Two surface treatment options intended to increase the strength of the adhesive bond were tested to determine their effectiveness. These surface treatment options included sanding the surface of the PVC and treating the surface of the PVC with corona arc discharge.

The sanding was accomplished by lightly scuffing the test surfaces with 220 grit sandpaper. After sanding, the sample was then wiped with dry paper towel to remove loose sanding debris. The sanding increases the surface area of contact between adhesive and plastic. Since some adhesives like the epoxy gain strength from mechanical interaction between the adhesive and plastic, increasing the effective surface area provides the adhesive with a more effective mechanical bond.

The second surface treatment was corona arc discharge. Corona discharge treatment involves running the corona arc across the surface of the plastic before application of adhesive. The corona arc discharge works to strengthen the adhesive bond by stripping electrons from the surface of the plastic. With the ionized surface, the adhesive chemically bonds to the plastic instead of mechanically. So while sanding increases the mechanical adhesion, corona discharge increases the chemical adhesion between the glue and plastic.

Effect of surface treatment for Acrylic Adhesive

The acrylic adhesive adheres to PVC in a manner different than epoxy. The epoxy adhesive has mild solvents which do not attack the surface of the PVC. In contrast, the acrylic contains solvents aggressive enough to melt the PVC slightly in order for the acrylic to mix with and bond to the plastic. Surface treatment of the PVC is not expected to have a noticeable effect on the strength of the acrylic bond as its own solvents are thought to have a greater effect than either sanding or corona discharge.

It is known from Nitti[7] that the strength provided by acrylic on untreated PVC is sufficient for constructing the detector. For this reason, when used in production of modules, the PVC has no surface treatment for the acrylic. To confirm this practice, it is desirable to know if acrylic surface treatment effects truly are negligible or significantly beneficial. Therefore, all of the acrylic samples at the nine month aging time were treated with either sanding or corona discharge. In order to make a direct comparison, new samples with and without surface treatment were tested.

2.2 Test Samples' Stress Loading Configuration and Preparation Details

This section discusses the stress loading configurations for the three sample types as well as the sample preparation procedures.

2.2.1 Strength Test Varieties and Specifications

The adhesive-plastic seams in the detector modules are placed in several states of stress by the variety of stress loading inherent to the detector. Because of this, it was desired that the chosen adhesives be strong under several loading conditions. Thus, samples

with tensile, shear, and cleavage-peel stress loading of the adhesive-PVC bond were prepared for testing. Figure 2.2 shows the stress loading of the three sample configurations.

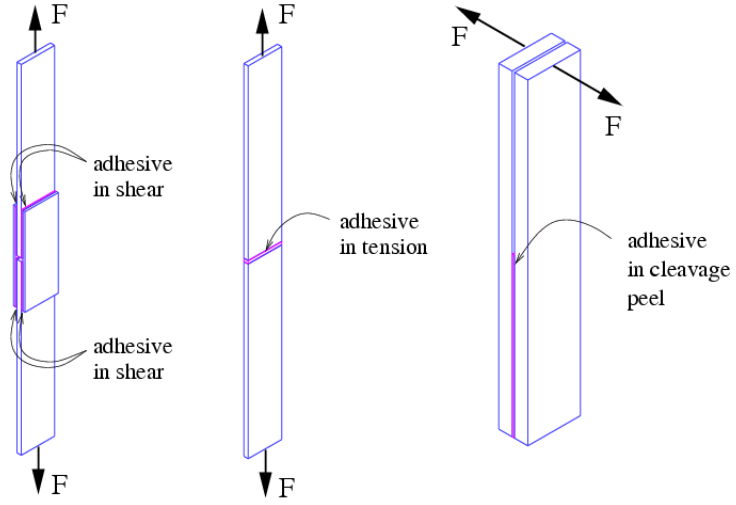

Figure 2.2: The stress loading configurations for the three sample types. From the left: shear, tension, and cleavage-peel.[5]

2.2.2 Sample Preparation

All samples were prepared from plastic sample blanks which were made from extrusion PVC plastic trimmed to 1 inch wide. The samples were then planed to 0.125 inch thick and cut to the appropriate length. Samples that were too thin or narrow were rejected.

The tensile samples test the tensile strength existing between the adhesive and plastic. The samples were made of two PVC pieces 100 mm by 25 mm by 3.2 mm (4" by 1" by 0.125"). The surface area of the tensile sample adhesive bond was 25 mm by 3.2 mm or 81 mm^2 (1" by 0.125" or 0.125" $inch^2$). Two PVC blanks were placed in line with each other with a spacing of 2 mm in between. The bottom of the gap was taped forming a well. This well was then filled with adhesive with care taken to ensure no air

bubbles were caught in the well. The adhesive was then leveled off with a straight edge, and the test sample given time to cure before removal from the sample preparation fixture. A detailed description of the sample preparation methodology is described on page 13 and following of Nitti[7].

All tested shear samples, aged and unaged with both adhesive types and surface preparations, exhibited failure of the PVC substrate prior to failure of the adhesive-PVC interface. Cleavage-peel samples results also lacked confidence as discussed in Section 2.4. As such, sample preparation techniques for shear and cleavage-peel sample types will not be elaborated here but are detailed in Nitti[7].

Time to cure

It was desired for the adhesives to be completely cured before testing their strength to ensure comparable strength to detector applications. The two primarily tested adhesives, acrylic and epoxy, have different cure times. From the work of Nitti[7], it is evident that in seven days, the epoxy will be fully cured; this is also the time specified by the 3M Technical Data sheet[8]. The acrylic will cure to working strength in 10-15 minutes and full strength in twenty four hours per its data sheet[9]. Thus, the acrylic samples were allowed to cure for at least two full days, and the epoxy samples for at least seven days to ensure complete curing.

Cooling time before testing

To ensure no heating effects skew strength data, all samples were stored in an controlled environment for three days prior to testing in accordance with ASTM standards for testing [10]. These standards require 23 $\pm$ 3 °C and 50 $\pm$ 5% humidity. All samples were subjected to this cooling time, even those newly made for the "zero time" tests.

The testing machines used are located in rooms without strict environmental controls. Though the conditions rarely exceeded the cooling specifications, care was still taken to limit the possible effects. To minimize the effects of these varying conditions, the samples were delivered to and kept in the testing room in sealed containers and used within an hour of leaving the temperature controlled room.

For the adhesive strength over time tests, to assure consistent testing conditions, all instances of the same type of test were performed on the same day. For example, all the cleavage-peel samples aged in the hot boxes and made fresh for the time dependence strength test were tested on the same day over a period of a few hours to minimize environmental differences in tests whose results are going to be directly compared. Tests were performed at the speeds specified by the ASTM and ISO standards for the strength tests [10], [11], [12].

2.3 Results

Two categories of variable were tested. The first examined the strength of the adhesive over time under various conditions. The second compared various sample preparation techniques for new, non-aged samples.

The results of the tests are reported and discussed in this portion of the chapter. Section 2.3.1 discusses the results of the studies on the acrylic adhesive, including strength versus time and surface treatment. Likewise, Section 2.3.2 provides the results of the epoxy adhesive studies.

As discussed in detail in Section 2.4, only tensile strength tests were used in the evaluation of the adhesives in this chapter. The shear stress samples adhesive strength exceeded the tensile strength of the PVC in nearly all cases, so the values measured did not allow comparisons of adhesive strength. Masking tape used in the cleavage-peel samples altered the strength of the joint invalidating the cleavage-peel results.

2.3.1 Acrylic Adhesive Strength Results

It was previously determined[7] that the strength provided by acrylic on untreated PVC was sufficient for building the detector. For this reason, when used in production of integrated prototype near detector (IPND) modules, the PVC underwent no surface treatment for the acrylic.

Some acrylic samples were aged in a hot box for nine months either dry or in scintillator oil. Some of these samples were treated with corona discharge and others were sanded.

Only tensile samples were used for this test. Prior tests of new acrylic samples in both shear and cleavage peel stress configurations saw failure in the PVC prior to failure of the acrylic-PVC interface. It was assumed that the various test configurations will generally follow the same strength versus surface treatment effect.

The results of the comparison of surface treatments for the acrylic are shown in Table 2.1 and in Figure 2.3. From these results, it appears that treating the surface of the PVC with corona discharge will increase the strength of the acrylic bond from 18.8 MPa to 21.2 MPa, about 14%. Sanding provided an even stronger initial bond than corona discharge, although the samples aged in oil displayed essentially the same strength as the samples treated with corona discharge.

Age and Surface Treatment	***Mean Failure Stress(MPa)***
Unaged, No surface treatment (10)	18.8 ± 0.8
Unaged, Corona Discharge (6)	21.3 ± 0.7
9 Months in Oil, Corona Discharge (5)	22.6 ± 1.6
9 Months in Air, Corona Discharge (5)	27.2 ± 1.2
Unaged, Sanded (6)	22.6 ± 0.5
9 Months in Oil, Sanded (5)	22.2 ± 1.0

Table 2.1: Acrylic surface treatment and aging tensile strength results listing the tensile mean failure stress and standard error of the mean. The number of samples in each data set is in parenthesis.

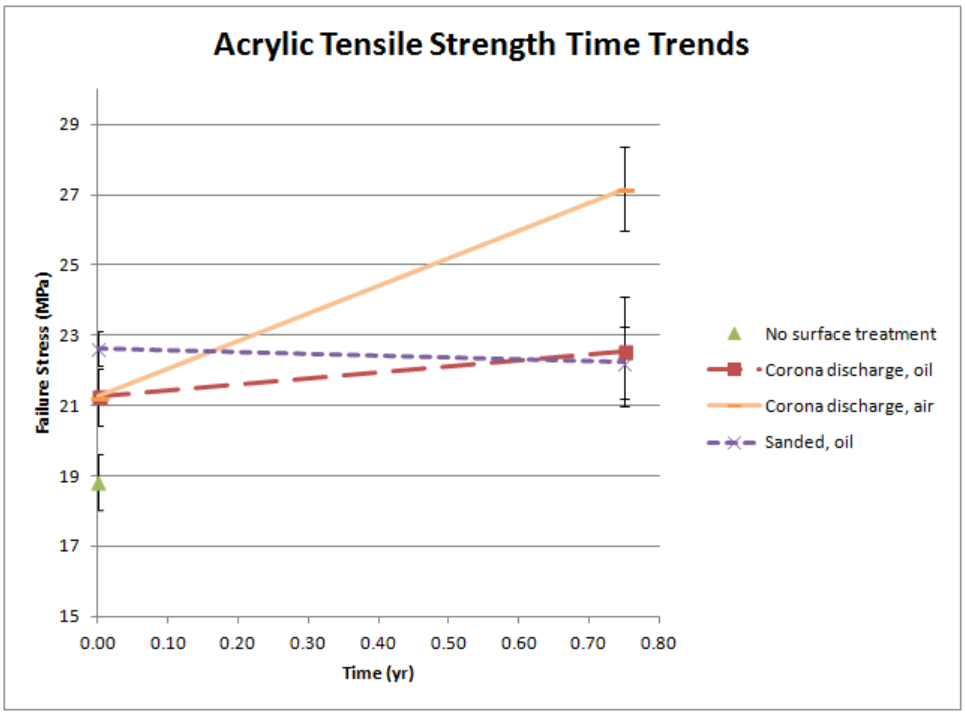

Figure 2.3: The tensile strength of acrylic adhesive for various surface treatment and aging conditions. The error bars show standard error.

2.3.2 Epoxy Adhesive Strength Over Time

In the dual adhesive seal design of the detector, the epoxy adhesive is used for the inner seal. While the primary purpose of the epoxy is to protect the scintillator from contacting the acrylic adhesive, the epoxy does add additional strength to the joint.

Some of the epoxy seams will be in contact with the scintillator oil for the life of the detector. To help understand how this aging would affect the strength of the epoxy bond, epoxy samples were aged in the hot box for a duration of 9 or 18 months, with samples in either air or in scintillator oil. The PVC surfaces of some samples were treated with sanding while others were treated with corona discharge.

Figure 2.4 and Table 2.2 show the tensile strength of the epoxy adhesive samples

after aging in the hot box. The unaged strength of both surface treatment options is similar.

Age and Surface Treatment	***Mean Failure Stress(MPa)***
Unaged, Corona Discharge (4)	11.3 ± 1.0
9 Months in Air, Corona Discharge (5)	12.6 ± 0.7
9 Months in Oil, Corona Discharge (5)	12.5 ± 1.0
Unaged, Sanded (4)	10.7 ± 0.6
9 Months in Air, Sanded (4)	10.1 ± 1.2
18 Months in Air, Sanded (5)	11.3 ± 1.2
18 Months in Oil, Sanded (4)	8.9 ± 0.9

Table 2.2: Epoxy surface treatment and aging tensile strength results listing the tensile mean failure stress and standard error of the mean. The number of samples in each data set is in parenthesis.

After 9 months of aging, the strength of the corona discharge samples aged in oil and air appear to have slightly higher strength than the sanded samples aged in air although there is not a statistical difference between any of the 9 month samples and the initial new samples.

After 18 months of aging, the sanded samples aged in air are still very similar to the new strength of the sanded samples. The sanded samples aged in oil did have a slightly lower measured strength than the new samples and the samples aged in air.

The strength of the epoxy adhesive samples was fairly constant over the aging period with the strength increasing slightly for most samples. Only the sanded samples aged in oil exhibited loss of strength and that by only 17%.

Corona discharge was chosen as a PVC surface treatment for construction of the NOνA detectors. While either sanding or corona discharge appeared to be acceptable, the corona discharge samples performed better both in aging in air and aging in scintillator oil.

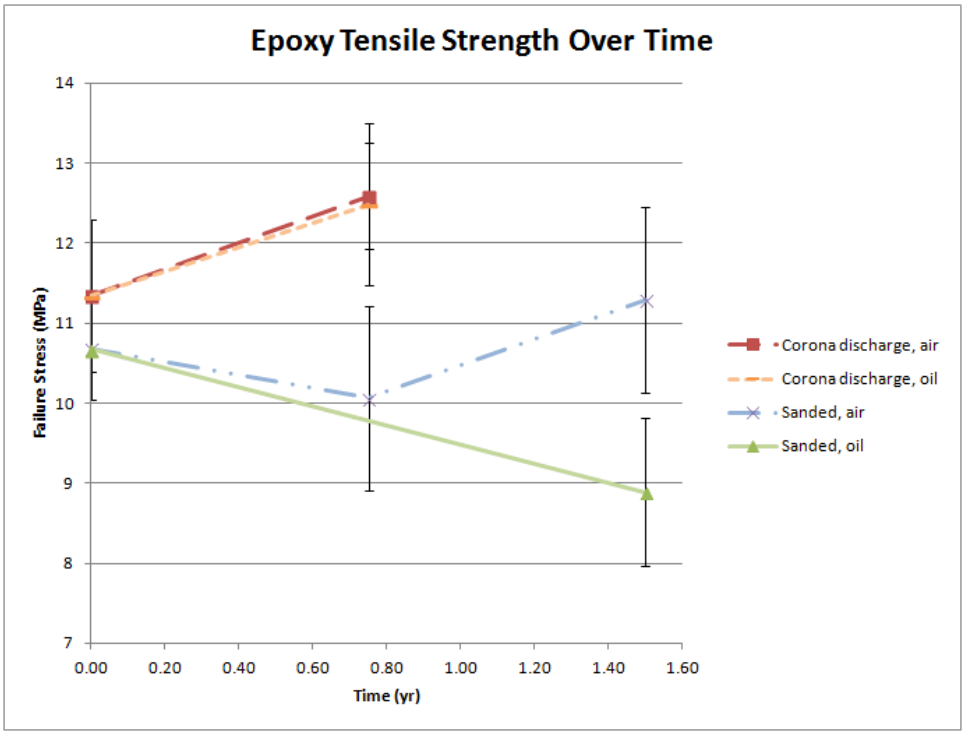

Figure 2.4: The tensile strength of epoxy adhesive for corona discharge and sanding surface treatment after aging in air or in scintillator oil. The error bars show standard error.

2.4 Shear and Cleavage-Peel samples discussion

Although samples were prepared to test both shear and cleavage-peel stress loading in addition to tension, the shear and cleavage-peel samples encountered compromising problems as described in this section and were thus discarded from the previous results sections.

2.4.1 Shear Test

A double-lap shear sample type based on ASTM Standard D3528[12] was selected to eliminate bending of the shear sample during testing as can occur with a single-lap shear

sample type (see Fig. 2.2). This double-lap sample type has twice as much adhesive surface area as a single-lap shear sample type but is symmetric thus eliminating bending of the samples.

The high surface area specified by the standard demands a high force be applied to reach the failure shear stress of the adhesive. As such, in samples of both the epoxy and the acrylic adhesives, aged and unaged, the PVC invariably failed in tension before the shear joint failed as seen in Fig. 2.5. While the failure of the PVC instead of the adhesive joint provides confidence that the adhesive is at least stronger than measured in Nitti's[7] comparison of adhesive varieties, it does not give quantitative data on shear strength trends caused by aging or being immersed in scintillator oil.

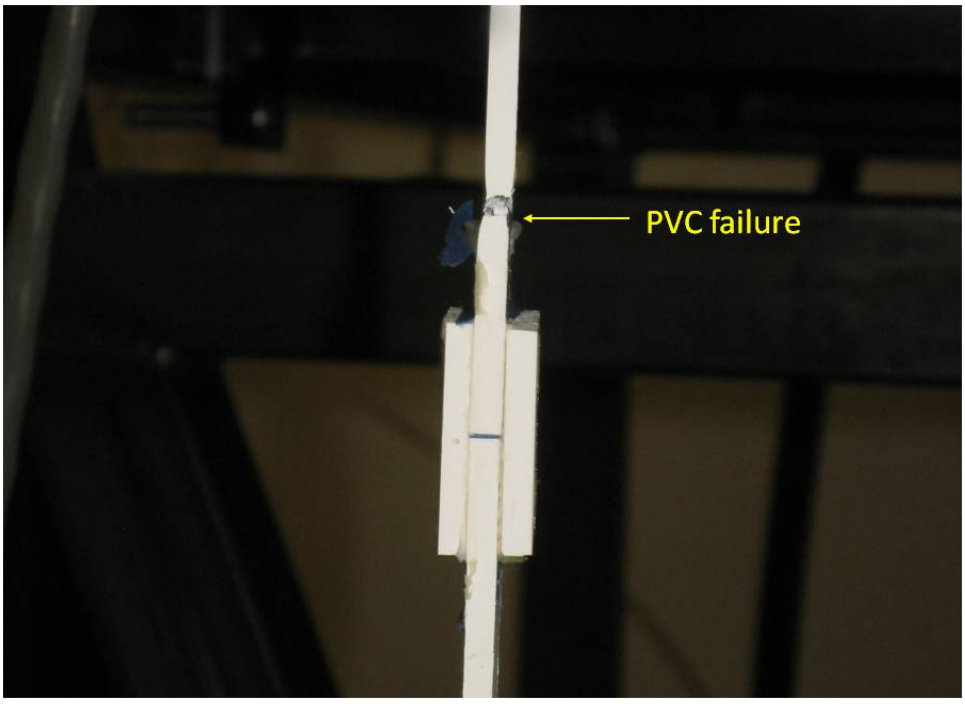

Figure 2.5: Failure of the PVC substrate before failure of the shear joint on an acrylic shear sample.

This allows us to be confident the adhesive is at least stronger than measured in Nitti's[7] comparison of adhesive varieties.

When testing the shear strength of the materials, all of the test specimens tested failed in the plastic grip portion of the sample and not the adhesive portion. Thus the strength measured corresponded to an ultimate strength of the PVC, not the shear strength of the adhesive.

These shear tests show that the adhesive strength is high compared to the PVC as the plastic failed before the adhesive, but the tests were unable to provide information on the effect of aging on the shear strength. As such, shear strength data will not be considered in the following discussion.

In the future, it would be good to test shear stress loading by adapting the ASTM standards to be compatible with the combination of adhesive and PVC used in the NOνA detectors. The shear samples could be adapted by reducing the adhesive surface area while persisting with the double-lap shear sample configuration. The shear samples intended to be used in this test were prepared with the same substrate dimensions used in Nitti[7] to select these specific adhesives from weaker adhesives.

2.4.2 Cleavage-Peel Test

Masking tape used to limit the area of the PVC the adhesive contacted ended up adding additional strength to the cleavage-peel joint in fresh samples and samples aged in air while the masking tape adhesive was dissolved on the samples aged in oil as seen in Fig. 2.6. As the values measured for most of the samples are affected by the preparation method, the cleavage-peel sample will be omitted from this discussion.

If cleavage-peel stress loading is tested in the future, the cleavage-peel sample could be prepared with masking tape with very low adhesion to assist in easy separation of the tape from the PVC during testing or by using a tape with a non-stick backing such

Figure 2.6: Effect of masking tape in cleavage-peel strength samples. The top image shows the masking tape adding additional strength to the cleavage-peel sample in an un-aged sample. The bottom image shows the masking tape having no effect after being aged in oil.

as PTFE to allow the tape backing to separate easily from the adhesive during testing.

2.5 Conclusion

In summary, Section 2.1 describes the variables being tested in the strength tests and the setup of the various tests, including accelerated aging for acrylic and epoxy adhesives with various substrate surface treatments. Section 2.2 discusses the modes of stress loading being tested as well as the sample preparation methods used in the testing. Section 2.3 reports the results of the acrylic and epoxy adhesive strength tests and discusses implications for construction of the NOνA experiment detectors.

There is opportunity to do more work on the subjects of this chapter. It would

be helpful to have control samples measured at room temperature to verify the heat accelerated aging guideline discussed in Section 2.1.1. This would allow strength test results to be extrapolated to real time more precisely and with more confidence.

Although all the strength tests described in this chapter use the extrusion PVC as the sample substrate, some of the joints in the detector have injection molded PVC as one of the components. It would be beneficial to repeat testing with this injection molded PVC to see if there is a suitably strong bond between the adhesives and the injection molded PVC.

Chapter 3

Interaction Studies for Liquid Scintillator Neutrino Detector Construction Materials

Many different materials are used in the construction of the NOνA liquid scintillator neutrino detector. Since the function of the detector is based on the effectiveness of the liquid scintillator filling the detector, care must be taken that none of the materials in contact with this liquid scintillator interact with it in a way that degrades the potency of the scintillator. Thus, all materials used in the construction of the detector must be tested for scintillator interaction.

This chapter explains how the interaction experiment works, how the experiment is set up, the results of the testing, and further potential work that could be done with this line of experimentation.

3.1 How the Scintillator Test Works

The detector is made up of PVC pipe sections filled with a liquid scintillator. This liquid scintillator is primarily made up of mineral oil while the active scintillator ingredient, pseudocumene, makes up 5% of the scintillator solution[13]. The mineral oil acts as a solvent for the pseudocumene and adds additional mass to the detector. Because the pseudocumene is the scintillating agent in the solution, it is thus the essential component. The testing described in this chapter looks at the effect of various materials on the efficacy of the scintillator solution. If the pseudocumene is degraded by interaction with the tested materials, the measured energy of a gamma source will also decrease in the test.

To test the interaction of pseudocumene liquid scintillator with the various construction materials, vials of liquid scintillator are prepared with a sample of a material in each vial as documented in Section 3.3. Each vial is exposed to a gamma source which produces energetic electrons via Compton scattering and the photoelectric effect. The energy of these electrons is converted by the scintillator into photons, which are measured with a photomultiplier tube (PMT). An alpha source in combination with plastic scintillator is used as a constant reference energy to normalize the liquid scintillator signal as the drift of the PMT signal can be significant. Each component of the testing setup is described in Section 3.2.

3.1.1 Compton Edge Midpoint

This test is designed to observe the change in efficiency of the liquid scintillator over time. In the case of this test, the scintillator is converting the energy from electrons Compton scattered by gamma rays into photons in the visible spectrum. This is then compared to the light output of the plastic scintillator excited with an alpha source.

The gamma rays interact with the scintillator solution via Compton scattering and

the photoelectric effect. In the photoelectric effect, the entire energy of the gamma ray is absorbed by an electron which is ejected with the same energy. In Compton scattering, merely a portion of the gamma ray's energy is transferred to the electron.

Compton scattering occurs when a gamma ray interacts with an electron and transfers some of the gamma ray's energy and momentum to the electron. The electron scatters away and the gamma ray continues off having a greater wavelength corresponding to the energy lost to the electron, as diagrammed in Figure 3.1.

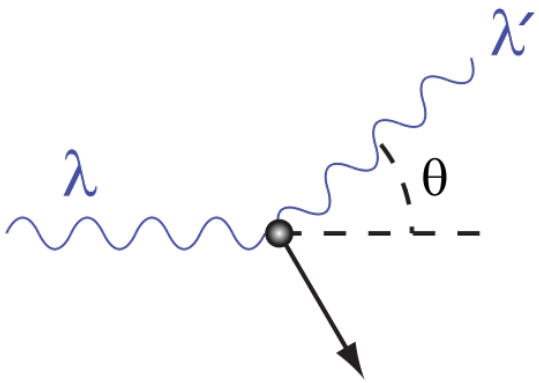

Figure 3.1: This diagram demonstrates the Compton effect as a gamma ray with wavelength λ scatters off an electron and continues on its way with a longer wavelength λ'. The electron is ejected and scatters containing the energy lost by the gamma ray.[14]

Since the fraction of momentum transferred by Compton scattering varies based on the directness of the collision, a range of corresponding energies are observed. This range goes from zero energy corresponding to a gamma particle deflection angle of zero up to the maximum value corresponding to a deflection angle of 180 degrees or full reflection. This maximum value is referred to as the Compton edge and is illustrated in Figure 3.2.

A second phenomenon, the photoelectric effect, also occurs when the gamma rays interact with the scintillator solution. In the photoelectric effect, the electron absorbs

all of the energy of the gamma ray instead of just a fractional amount. The photoelectric effect results in a peak of greater energy than the Compton edge as all of the gamma ray energy is absorbed.

As the electron scatters through the scintillator material, the energy from the electron is deposited into the scintillator. This energy causes electrons in the scintillator molecules to be excited to higher energy orbitals. When these electrons relax back down to lower energy states, they emit photons in the visible spectrum with an energy corresponding to the electron orbital energy difference. The number of photons produced by the scintillator corresponds to the transferred energy. These photons travel through the scintillator onto the photocathode surface of the PMT. The PMT then outputs a current corresponding to the energy of the scattered electron.

In the testing and analysis detailed in the following sections of this chapter, the Compton edge is used as a part of a ratio to determine the degradation of the scintillator. The Compton edge is defined as the midpoint of the edge of the apparent Compton peak seen in Figure 3.2, that is the point at the full width half maximum (FWHM) of the distribution of the Compton edge. The FWHM value on the curve is the position on the curve that has half the maximum value of the Compton peak on the full width of the curve of the Compton edge. In reality, the system used does not have a perfect resolution to capture the full details of the gamma source energy spectrum. As such, the Compton edge seen in the energy histograms and used in ratio calculations in Section 3.4.2 is a superposition of the Compton edge and the photopeak. An example of this superposition is illustrated in Figure 3.2.

The Compton edge midpoint is calculated from the position of the Compton peak and the width of the Gaussian curve fitted to the superimposed photopeak and Compton edge. The Compton edge midpoint is the energy value on the Compton peak curve that has half the maximum peak value. The formula for the calculation of the Compton

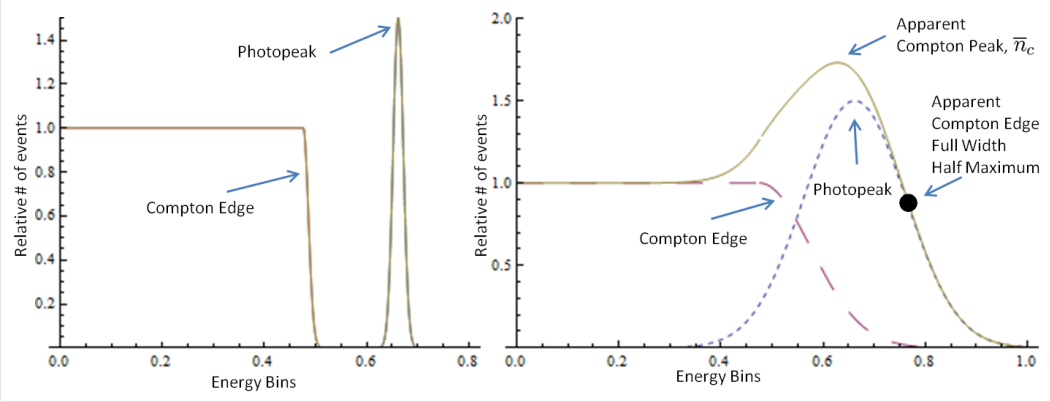

Figure 3.2: The left plot shows a distinct Compton edge and photopeak. The plot on the right shows the curve resulting from the superposition of the Compton edge and photopeak with a system that has a lower energy resolution such as that used in the testing in this chapter. This superposition peak will be called the "Compton peak" in this report. The labeled "Apparent Compton edge" is the full width half maximum of this Compton peak and will be the energy position refered to as the "Compton midpoint".

midpoint follows in Equation 3.1 where $\overline{n}_c$ is the apparent Compton peak as illustrated in Figure 3.2 and σ_c is the standard deviation of the Compton peak distribution.

$$\text{Compton Edge FWHM} = \overline{n}_c + \sqrt{2\ln 2}\,\sigma_c \tag{3.1}$$

3.1.2 Alpha Peak

The other half of the testing system includes an alpha source and a solid plastic scintillator. The purpose of the alpha source is to provide a consistent energy peak to which the Compton edge can be compared. A plot showing both the Compton edge and the alpha peak can be seen in Figure 3.3.

The alpha peak will always correspond to a consistent energy level as every alpha interaction will produce the same amount of light in the solid scintillator and thus

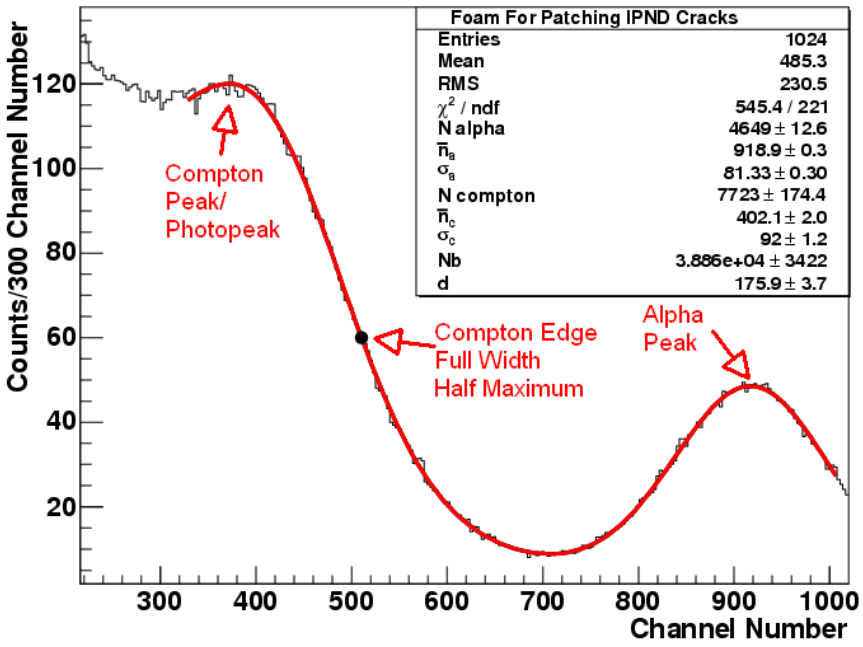

Figure 3.3: This plot shows several features of a typical energy histogram for the interaction test including the Compton edge, the alpha peak, and the Compton-photopeak as discussed in Figure 3.2.

the PMT. This allows the alpha peak to be used as a control against changes in the PMT due to temperature and other variables. The position of the alpha peak and the position of the Compton edge are the primary values used in the analysis in this chapter. The ratio of the Compton edge to the alpha peak is monitored over time. This ratio should remain constant if the sample material being tested has no interaction with the scintillator liquid and should decrease if an interaction is occurring.

3.2 Test Apparatus Setup

A piece of solid plastic scintillator is used together with the alpha source to provide a normalization reference for the Compton edge measurement. The plastic scintillator is the same as that used in the MINOS neutrino detector. The scintillator is extruded polystyrene doped with 1% PPO (2,5-diphenyloxazole) and 0.03% POPOP (1,4-bis(5-phenyloxazol-2-yl)benzene)[15]. The plastic scintillator is transparent and has a white reflective coating on the top surface to direct as much light produced by the alpha source energy to the PMT as possible to maximize the signal to the PMT window. This coating has a similar purpose as the white PTFE tape layer around each test tube sample described in Section 3.3 which is to increase the signal strength and help the maximum amount of light from each interaction reach the PMT so that the signal is not dependent on the location in the scintillator where the alpha interaction took place.

A disc of scintillator the diameter of the PMT surface is fabricated. The scintillator lies flat on the PMT photocathode surface and covers the full surface of the PMT. A through hole in the plastic scintillator the diameter of the test vial allows the bottom of the test vial to interface directly with the PMT surface. A blind hole is cut about half way through the solid scintillator and holds the alpha source in close contact to the solid scintillator allowing as many alpha particles as possible to interact with the scintillator and provide a strong alpha signal to the PMT. These features can be seen in Figure 3.4 which shows the test enclosure setup.

A sample, which is contained in the glass vial, is placed in the designated hole in the solid scintillator. The sample is prepared as detailed in Section 3.3.

The gamma source is positioned on the outside of the test chamber corresponding to the location of the sample inside the test chamber. This allows the maximum possible interactions from the gamma rays in the test sample.

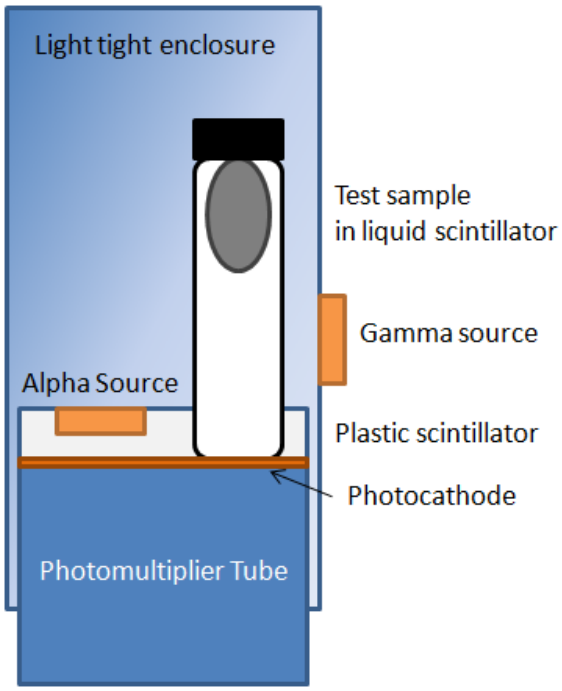

Figure 3.4: The components of the scintillator test enclosure.

3.3 Sample Preparation

Many types of materials were tested, and the sample acquisition and preparation varies somewhat for each material category. The goal in the sample preparation is to provide the maximum sample surface area per test volume in order to achieve a strong interaction if an interaction occurs. This will allow the most rapid detection of incompatible materials and aid in subsequent material selection.

All PVC samples, cutting tools, and materials were cleaned with isopropyl alcohol (IPA) prior to testing as well as possible. Nitrile gloves were worn to minimize skin oil contamination of samples.

A stainless steel mesh basket was used to contain the sample material in each of the interaction tests. A mesh tube lint collector was used to create this basket. The lint

collector was cut into approximately two inch long sections. Each section of mesh tube was crimped on both ends to create the basket containing the sample. To ensure there was no interaction with the mesh, a control sample containing only the mesh basket was tested.

For each material, a decision is made on the optimal method for maximum surface area per volume for testing.

Many adhesives are being used in the detector. Some adhesives such as the acrylic used to attach the end caps to the module are very strong and are impossible to separate from their substrate. Thus, they are applied in a layer to a PVC tested and known to have no interaction with the scintillator. This composite is then punched into 6.4 mm circles or snipped into small pieces with metal shears.

Less strong adhesives which function as rigid gaskets on the module end caps and manifold covers are applied in a layer onto the PVC like the above acrylics. Once cured, they are then separated from the PVC backing and cut into small pieces with a scissors or metal shears.

Various varieties of PVC and other plastics were tested. For PVCs in block form, a block plane was used to shave long slivers off the corner edge of the block. These pieces were then cut into approximately 1 cm lengths for testing. For PVCs and other plastics in sheet form, the sheets were cut into small pieces about 2 mm by 10 mm.

Paste or gum-like materials such as PTFE paste were deposited directly into a steel mesh basket as they are thick enough to not leak through the holes in the mesh.

For thin tapes such as PTFE tape, a length of tape was loosely folded and placed into a mesh basket.

A ball valve which is used to empty the vertical sections of the prototype near detector needed to be tested. The valve was disassembled into individual pieces. The various seals, bearings, and other small loose valve pieces were collected into a mesh

basket to be tested. The metal valve outer housing was too large to fit into the vial. A hacksaw blade was first cleaned with isopropyl alcohol then used to cut the valve into smaller pieces that would fit in the vial. In order to keep all grease or other residues from the valve intact, the resulting pieces were not cleaned with IPA.

A photograph with a partially completed sample of a PVC test as well as a complete sample can be seen in Figure 3.5.

Figure 3.5: A interaction study sample of PVC in various stages of preparation. On the left, the shaved PVC is enclosed in the stainless steel mesh. On the right, the sample has been wrapped with PTFE tape and filled with scintillator.

To fill each sample vial, 30 mL of 4% pseudocumene in mineral oil scintillator oil is obtained from a 55 gallon drum. First, a 50 mL beaker is cleaned with IPA and paper

towels. Next, a clean meter long stainless steel tube with an outer diameter of 6mm is used to pipette 30mL of scintillator from a 55 gallon drum into the clean beaker. This scintillator is then poured from the beaker into the vial with a prepared test sample ensuring the sample material is submerged.

White PTFE tape is wrapped on the outside of the vial covering the entirety of the outer surface aside from the bottom as seen in Figure 3.5. The PTFE tape serves to reflect photons back into the scintillator and thus increases the chances of the photons hitting the PMT. This reduces differences in photon quantities detected by the PMT from variations in interaction location in the test vial.

In order for the fit to work correctly, there must be a space in the energy bin histogram between the Compton edge and the alpha peak as can be observed in Figure 3.3. With no adjustment, the Compton edge will often overlap with the alpha peak and cause errors in the fit similar to that in Figure 3.7. To increase this necessary energy gap, a small piece of electrical tape is placed on the bottom of the test vial to block a portion of the light produced by the scintillator. This tape thus serves to reduce the light seen by the phototube from the gamma source in the test sample in comparison to the unaltered alpha source and increase the gap on the histogram.

A cotton string is tied around the neck of the vial to assist in placement into and removal from the testing chamber.

Each sample is labeled on a piece of masking tape which is placed on the lid of the vial. A mark on this label also is used for angular alignment of the test vial in the test chamber. This allows approximate realignment in subsequent tests of the same sample.

Once a sample is prepared, the sample is placed into the testing chamber as soon as possible after the scintillator oil has been added to the sample. This allows data to begin to be collected as quickly as possible which enables the capture of any rapid interaction effects and sets a base value for ratio of Compton edge to alpha peak.

3.4 Testing and Analysis

In Sec. 3.4.1, the methods used to acquire a series of energy histograms for each sample are described. In Sec. 3.4.2 analysis of the energy histograms obtained in Sec. 3.4.1 provide the Compton edge midpoint and alpha peak locations for each histogram, the values of which are used to determine scintillator deterioration.

3.4.1 Data Acquisition

Each test of a sample is done by the following procedures: First, a sample is prepared and placed into the testing chamber. The top of the test chamber is securely attached to block any light leakage from outside the test chamber. Data collection is initiated and the real time data collection is viewed on an oscilloscope to visually confirm that the Compton edge and alpha edge are distinct from each other to allow the fit to work correctly. If overlap occurs between the Compton edge and alpha peak, data collection is interrupted, the sample removed, and a slightly larger piece of electrical tape is affixed to the bottom of the test vial to reduce the measured energy of the Compton edge signal slightly as discussed in Section 3.3.

The DAQ system has 1024 bin counters which correspond to the range of energies of the Compton scattering and alpha events. For each gamma or alpha event observed by the PMT, the PMT outputs a current pulse corresponding to the energy of that event. This current is measured by the DAQ which then increments the bin counter corresponding to that event energy.

While each test runs for several days, data are collected in shorter increments. This increment is specified during the setup of the test and is generally between 10 and 30 minutes in length. The data collected during each increment is fitted with a curve which identifies the Compton edge midpoint and the alpha peak location. The ratio of the Compton edge midpoint to the alpha peak location is plotted and compared to previous

and subsequent increment ratios. Data are usually collected for 50 to 300 increments depending on the test setup. For the same duration test, shorter collection intervals for each datum point allow more data points to be plotted while longer collection intervals reduce noise in the data and allow a better fit.

Data for a particular test are collected for several days at a time. Results can be seen in the first day for test materials that obviously interact with the scintillator such as the acrylic used to attach the module ends. Data are taken for 3 to 14 days for most samples to give the material adequate time to interact with the scintillator.

3.4.2 Data Analysis

Running the fit on a data set will provide the value of the alpha peak and the Compton peak as well as the standard deviation of the Compton peak. Once the Compton edge is calculated as discussed in Equation 3.1, its value is compared to the alpha peak. This ratio of the Compton edge to the alpha peak location comprises a single datum point used in the analysis.

The series of ratio points are plotted against time to access how the ratio changed over time. If the ratio remains generally constant, it shows that the sample material is not interacting with the scintillator nor harming its light output. If the ratio decreases, it demonstrates that the sample material is interacting with the scintillator, and the material is deemed unfit for use in the detector. If the behavior of the ratio over time is not clear, a new sample is prepared and tested as discussed in Section 3.5.

To more easily visualize changes in the ratio, the data set is normalized by an initial ratio value. This process allows the general scatter of the ratio points to be centered around 0% change at the beginning of the test. As the test progresses, changes to the initial ratio can then be observed and more easily quantified.

To normalize the ratios, each ratio is divided by a value that centers the initial

scatter of ratio values around the value 1. Next, 1 is subtracted from each new ratio value which centers the initial ratio values around zero. This effectively results in each ratio value now showing its percent change from the initial ratio value. This allows simple viewing and comparison of the ratio values and also indicates clearly the scale of any changes.

Occasionally, individual ratio values will vary greatly from the mean. This usually indicates that there is an error in the fit or in the data collection. If the fit visually appears to be poor, the calculated ratio for that sampling period is discarded from the analysis. Poor fits are usually quite obvious as the ratio of the Compton edge to the alpha peak often is quite extreme. If the fit looks accurate but the particular ratio value is still far off of typical, that datum point is not discarded from the analysis.

Most often, a poor fit results from counts being dropped by the DAQ in certain energy bins during sampling. The histogram of the bin counts of the energy levels will show gaps in the data as shown in Figure 3.6.

Occasionally, the histogram will have some peculiarity in the Compton peak or alpha peak which does not allow an adequate fit to be achieved as shown in Figure 3.7. This can happen when the scintillator deteriorates as a test progresses.

3.5 Results

Once the normalized ratio values have been obtained, these normalized values are plotted against time. This plot is then examined to see if the signal decreases with time which would indicate a deterioration of the scintillator.

To aid in the determination of signal degradation, a moving average is calculated and displayed along with the individual data points. This trend line allows clearer visualization of trends in the scintillator performance.

The selected moving average includes the value for the sample time as well as the

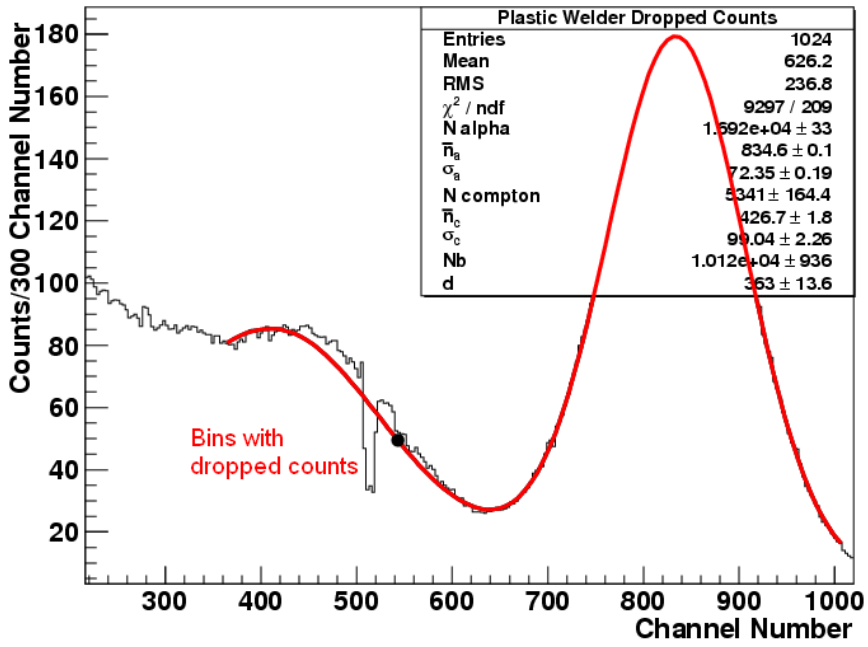

Figure 3.6: This histogram of the energy bins shows where counts were dropped in the sampling and the resulting skewed fit of the energy curve.

values for the nine sampling time periods preceding and following the current sample time. Examples for degrading scintillator, stable scintillator, and an indeterminate test are provided below.

3.5.1 Example of Failure for Interaction Test

An example of a material that failed the test and was deemed unfit for use in the detector construction was a PTFE paste used in pipe fitting. Figure 3.8 shows the plot of the Compton edge midpoint to alpha peak normalized ratio values versus time. The diamond points are the ratio values while the line shows the moving average values. The decrease in the value of the ratio can be clearly seen as the ratio dropped 14% in

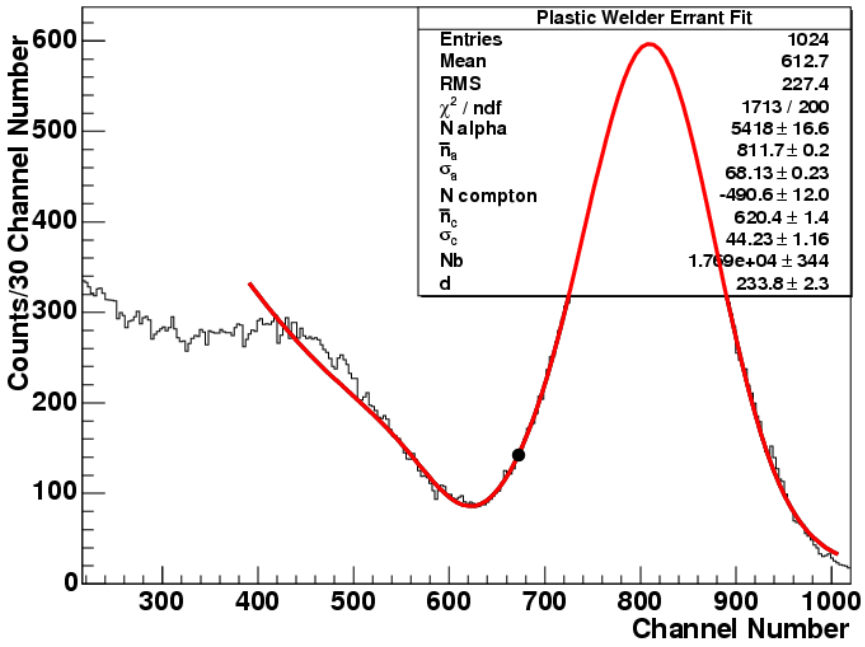

Figure 3.7: This histogram of the energy bins shows a flawed fit in a sample with deteriorating scintillator.

less than 24 hours.

3.5.2 Example of Passing for Interaction Test

An example of a material that passed the test and was allowed in the construction of the detector was PTFE tape used to seal the drainage valve for the vertical modules used in the integration prototype near detector. As can be seen in Figure 3.9, the normalized ratio of the Compton edge midpoint to alpha peak remains relatively constant over a duration of eleven days. This demonstrates that the PTFE tape does not interact with the scintillator and is thus acceptable to use in the detector.

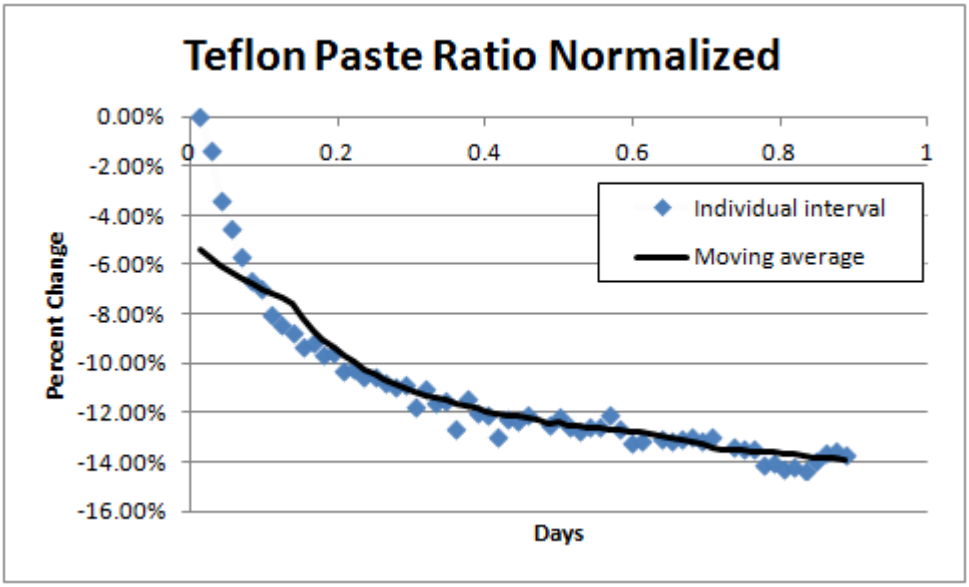

Figure 3.8: This plot shows the normalized ratio of Compton edge midpoint to alpha peak for a PTFE paste. The downward trend of the ratio values clearly indicates interaction of the PTFE paste with the scintillator.

3.5.3 Example of Ambiguous Interaction Test

Occasionally a test will produce ambiguous results for a material. This may be caused by various environmental changes in the testing area, accidental bumping of the testing setup, sample contamination during the sample preparation, or other indeterminable factors. In the case of an ambiguous test, the material is retested.

An example of an ambiguous case is shown in Figure 3.10. In this example, a block of a PVC that will be used to attach the drain valve to the vertical modules used in the integration prototype near detector is being tested. The ratio remains constant for about 12 hours then drops about 1.5 percent over the next 12 hours before restabilizing and remaining constant for the last 48 hours of the test. The value of the ratio decreases about 1.5 percent over the duration of the test which could indicate an interaction with

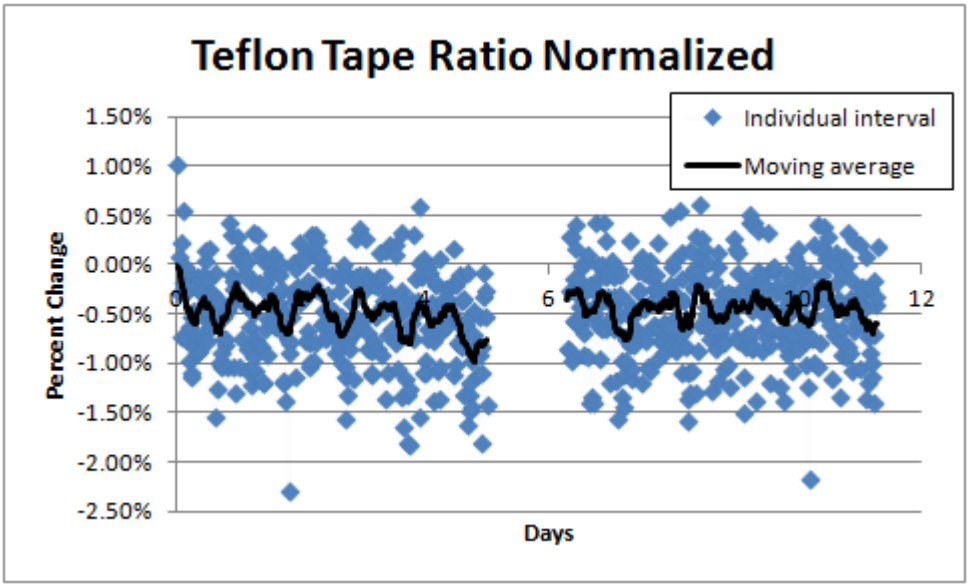

Figure 3.9: This plot shows the results of a PTFE tape. The steadiness of the ratio over 11 days indicates there is no interaction of the PTFE tape with the scintillator.

the scintillator and a failure of the test. But generally, a failing sample tends to exhibit continued and gradual ratio decline instead of steadiness followed by a rapid decline followed by steadiness. Since the sample in Figure 3.10 does not show steady and continued decline, the observed decline may not indicate interaction but some other factor. Thus the result is ambiguous, and the material should be retested.

Since the results are deemed ambiguous, a second test is performed on the same material. The results of this second test are shown in Figure 3.11. The ratio in the second test remained constant for 4.5 days and showed the material did not interact with the scintillator thus passing the test and being allowed in the detector construction.

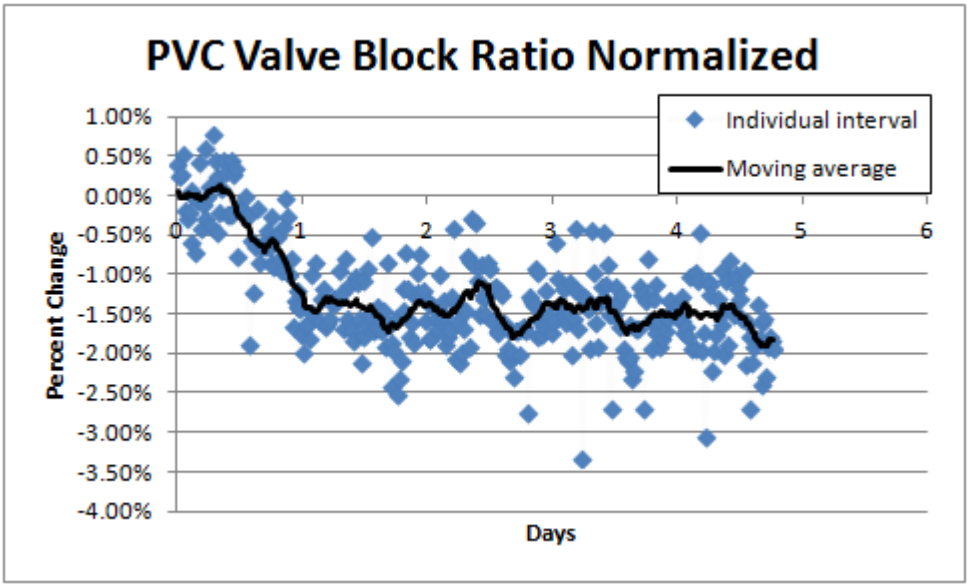

Figure 3.10: The results of the first test of a PVC used to house the drainage valve in the vertical modules. Since the ratio has an initial flat period followed by a rapid drop then another flat period, the test was deemed inconclusive and retested as shown in Figure 3.11.

3.5.4 List of Results for Specific Materials

Table 3.1 lists the interaction test results for many materials for potential use in the detector. Appendix B shows the ratio plots used to make these determinations.

3.6 Further Work

The testing for the NOνA project described in this chapter was intended to determine if various materials are suitable for use in the construction of a liquid scintillator pseudocumene based neutrino detector. As such, only binary type results were obtained from the tests as each test material either passed or failed the test.

Further work is being done to quantify results from the testing to determine how

Material	**Pass or Fail**	**Test Duration**
Adhesives		
2216 Epoxy	Pass	3 days
2216 Epoxy with Dye	Pass	5 days
Plasticwelder Acrylic	Fail	2.5 days
5 Minute Epoxy	Pass	5 days
DP 100 Epoxy	Pass	11 days
DP 420 Epoxy	Pass	4 days
Arrow Hot Glue	Fail	1 day
Tool Shop Hot Glue	Fail	1 day
PVCs and Plastics		
PVC for Valve Block	Pass	4.5 days
UV-Resistant PVC for Valve block	Pass	4 days
Fill Tube PVC	Pass	1 day
Raceway Cover PVC	Pass	2.5 days
Geon M3500 PVC	Pass	11 days
Fiber Tray PVC	Pass	8 days
Miscellaneous		
PTFE Tape	Pass	11 days
PTFE Paste	Fail	1 day
Globe valve housing	Pass	6 days
Globe valve internals	Pass	10 days

Table 3.1: The interaction test test results for many materials for use in the NOνA detectors. A pass means the material did not show interaction while a fail shows that the material did interact and should not be allowed to contact the scintillator in the detector. The duration of each test is also provided. Plots of each test result can be seen in Appendix B.

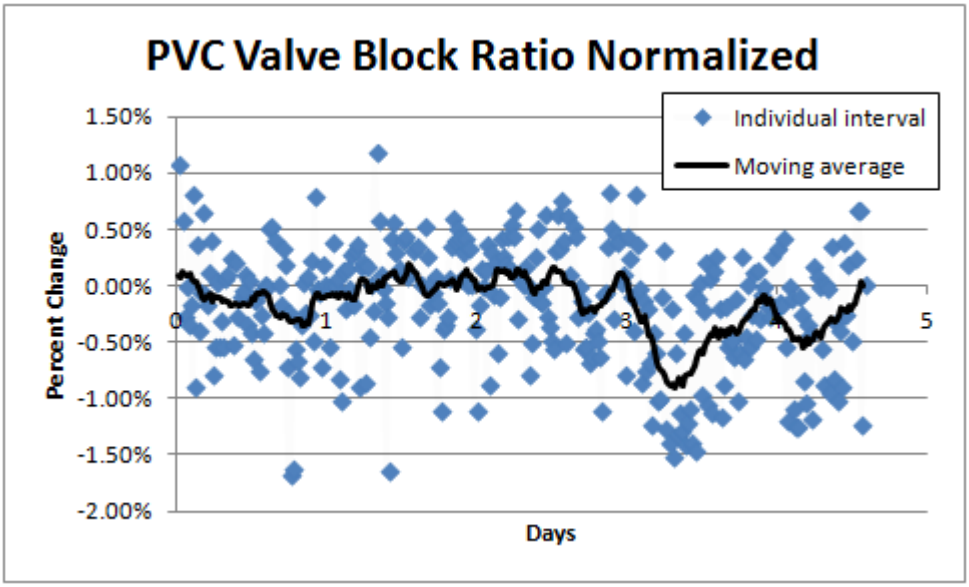

Figure 3.11: The results of the retest of the PVC initially tested in Figure 3.10. The steadiness of the ratio indicates that no interaction is taking place and the first test had some error in the testing.

strongly the various materials interact with the scintillator. These tests are being carried out with controlled material surface areas and should be able to provide publishable results instead of a simple pass or fail rating.

For materials already known to interact with the scintillator, this testing method was able to observe interacting in a time frame of days instead of previously weeks or months. As such, most tests were run for a maximum of one week although several went for about two weeks. It would be desirable to run some long term tests on the materials most prevalent in the detector such as the extrusion PVC, the manifold cover PVC (Geon M3500), and the epoxy used as a gasket material in the manifold ends (3M 2216).

Chapter 4

Studies on Injection Molded PVC Strength, Stress Concentration, and Crack Initiation

Many parts of the NOνA liquid scintillator neutrino detector are made from injection molded PVC. Most of these injection molded parts are not designed to undergo stress once installed in the detector (the exceptions are the side and end seals on the end plate of the vertical modules which will see about 1.4 bar). While not specifically designed to withstand stress, the manifold cover and snout front and back undergo some stress during the assembly process. Because of this experienced stress, these parts may be weakened and form cracks. This stress primarily occurs during the pressure testing phases of the construction as the modules are pressurized with air to detect any leaks in the seals.

When Integration Prototype Near Detector (IPND) modules were constructed into a block at Fermilab, cracks were observed forming through the manifold cover after filling the IPND with oil. This chapter describes various experiments to learn more about the

cracking and develop strategies to mitigate the risk of cracks forming in far detector modules.

The cracks were mostly observed occurring at Rib 3 of the manifold cover on the side of the rib opposite the snout. A cross section of the manifold cover at Rib 3 is shown in Fig. 4.1. This figure also shows the position of the ribs on the manifold cover and relationship to the snout. The manifold cover was originally molded out of Geon M3800 PVC, as was the snout, and end and side seals.

Figure 4.1: On the left, a cross section of the manifold cover at Rib 3. On the right, a lengthwise cross section photo of the manifold cover and snout with the rib locations labeled.

This chapter includes three main sections investigating the cracks in the manifold cover. The first, Section 4.1, describes the measured tensile strength of a new manifold cover made from Geon M3800 PVC. These measurements provide information about the nominal strength of the pre-assembled manifold cover and variation in strength due to manufacturing processes.

Section 4.2 deals with stress concentration in Geon M3800 and M3500 PVC with right angle sections from the snout back. Observations are made about the nature of the

observed PVC failure. A comparison is done between the originally used Geon M3800 and Geon M3500 with the Geon M3500 seeming to be a better choice for the manifold covers.

Finally, Section 4.3 describes the studies into crack initiation and propagation in the manifold covers. The role of the pressure test in the formation of cracks in the manifold covers is studied and discussed.

4.1 PVC Material Properties

Manifold covers for the IPND were observed to crack at the third rib when constructed into a block at Fermilab. It was desired to determine if weak PVC at this location might be contributing to the cracking. The tensile strength of the manifold cover PVC was measured in various locations on the manifold cover including multiple times across Rib 3. The strength of the Rib 3 samples was compared to strengths from the top and sides of the same manifold cover to find abnormalities in the Rib 3 strength values. The elastic modulus was also calculated from the stress versus strain curve and compared to the vendor's published value.

Section 4.1.1 describes how the tensile test PVC samples were obtained from a new manifold cover. Section 4.1.2 explains the testing methodology and apparatus. Section 4.1.3 shares the tensile strength and modulus of elasticity measurements from the various sample locations and orientations.

4.1.1 Sample Setup

In order to test the tensile strength of the manifold cover at Rib 3, samples were cut from a new standard IPND manifold cover made from Geon M3800 injection molded PVC. ASTM D638, Standard Test Method for Tensile Properties of Plastics[16], was followed as closely as possible.

This standard calls for the tensile samples to be formed to a dogbone shape as seen in Fig. 4.2. This dogbone shape ensures that the maximum stress and fracture of the sample will be in the narrow testing region. The stress will be even across the narrow test section and will cause an even strain throughout the section. This strain is measured with an extensometer to acquire load versus extension data. This data can then be used to determine material properties such as ultimate strength and elastic modulus.

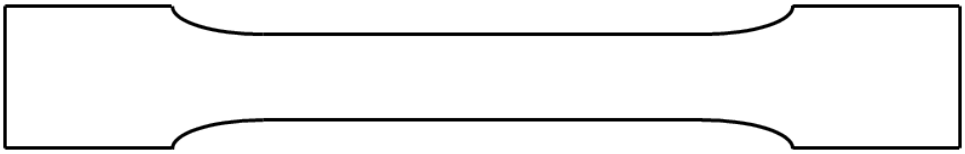

Figure 4.2: A general dogbone shape of the test sample for measuring the tensile properties of plastics as specified in ASTM D638 Standard Test Method for Tensile Properties of Plastics[16].

Unfortunately, the geometry of the manifold cover and the desire to obtain many test samples in close proximity to each other did not allow the practical obtainment of dogbone shaped samples without compromising PVC integrity. Instead, portions of the manifold cover were cut into 6 mm (0.25 in.) wide strips at least 125 mm in length. Since the stress amplification in the dogbone geometry that ensures the maximum stress and thus fracture will occur in the region measured by the extensometer is missing, the fracture may occur outside the range of the extensometer in the following tests. This could result in the strain appearing artificially low as is discussed in Section 4.1.3.

In order to observe the strength profile along Rib 3, as many samples as possible should be obtained across the rib. Samples were obtained by using a chop saw to slice the Rib 3 portion of the manifold cover into ten 6 mm strips. These samples were perpendicular to Rib 3. These samples were also perpendicular to the flow direction of the injection molded PVC. The PVC is injected along the back bottom edge of the

manifold cover and flows from the back of the manifold cover across the top to the front of the manifold cover where Rib 3 is located.

Additional samples were taken from the front, back, and top of the manifold cover both parallel and perpendicular to the direction of PVC injection flow. These locations are shown in Fig. 4.3.

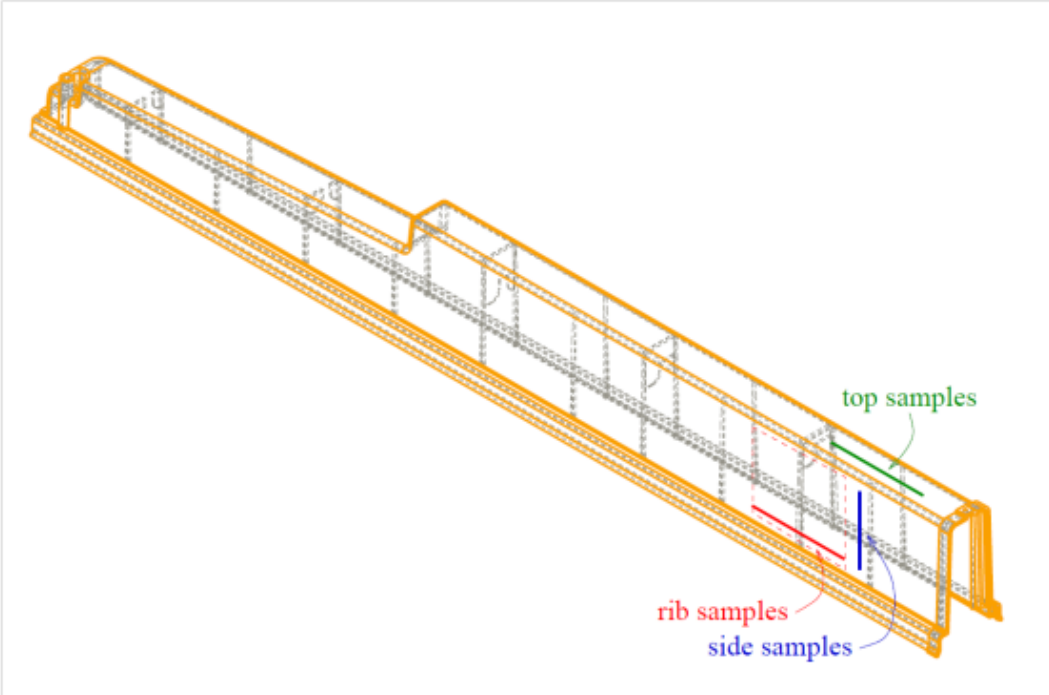

Figure 4.3: The locations on the manifold cover from which the tensile strength test samples were taken.

4.1.2 Testing

All testing conformed as closely as possible to ASTM standard D638[16]. The samples were conditioned at 24 ± 2 °C and 50 ± 5% relative humidity for 48 hours prior to being tested.

The samples were held in place by screw grips tightened by hand. The grips were positioned with a space of 57 mm (2.25 in.) between them. The extensometer used to measure strain had a 25 mm initial separation distance and was centered on each sample between the grips as seen in Fig. 4.4.

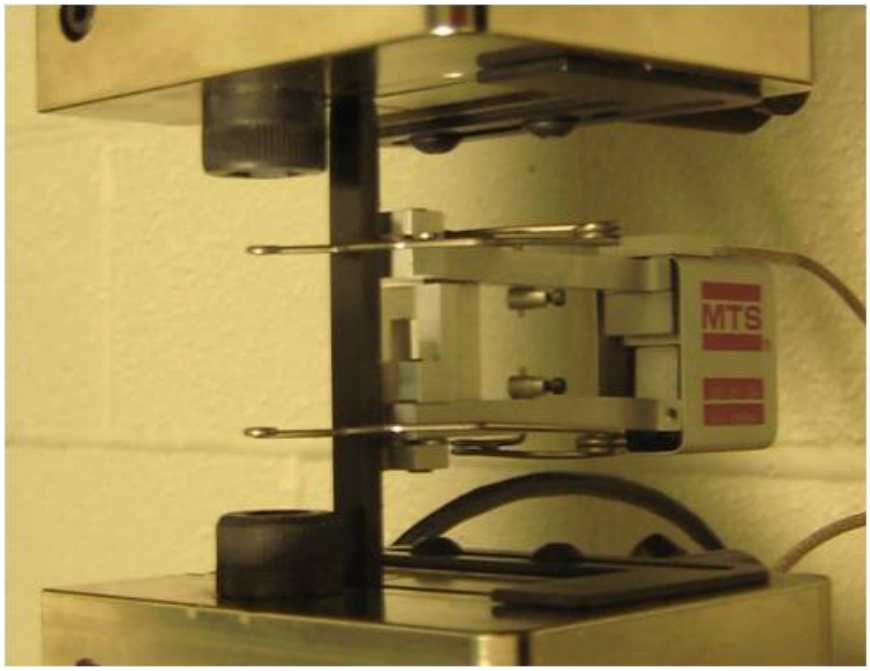

Figure 4.4: A manifold cover strength sample with the extensometer in place for testing.

A 1000 N load cell was used to measure the loads applied to the sample. These load data were later used to calculate the maximum stress on each sample by dividing by the average area. To calculate the cross sectional area of each sample, several thickness and width measurements were taken with a micrometer and averaged to find a reasonable representative value.

All samples were tested according to ASTM standard speeds at a crosshead speed of 5 mm/minute in an MTS QTest machine. The load and extension data were recorded

by a computer for analysis.

4.1.3 Results

The tensile test provided tensile load versus displacement data for the full testing cycle of each sample. The tensile load value of each sample was converted to tensile stress by the dividing the load by the nominal cross sectional area of the sample, providing the "engineering stress." The displacement was converted to engineering strain by dividing the displacement of the extensomenter by its initial separation distance. A plot like that shown in Fig. 4.5 could then be formed.

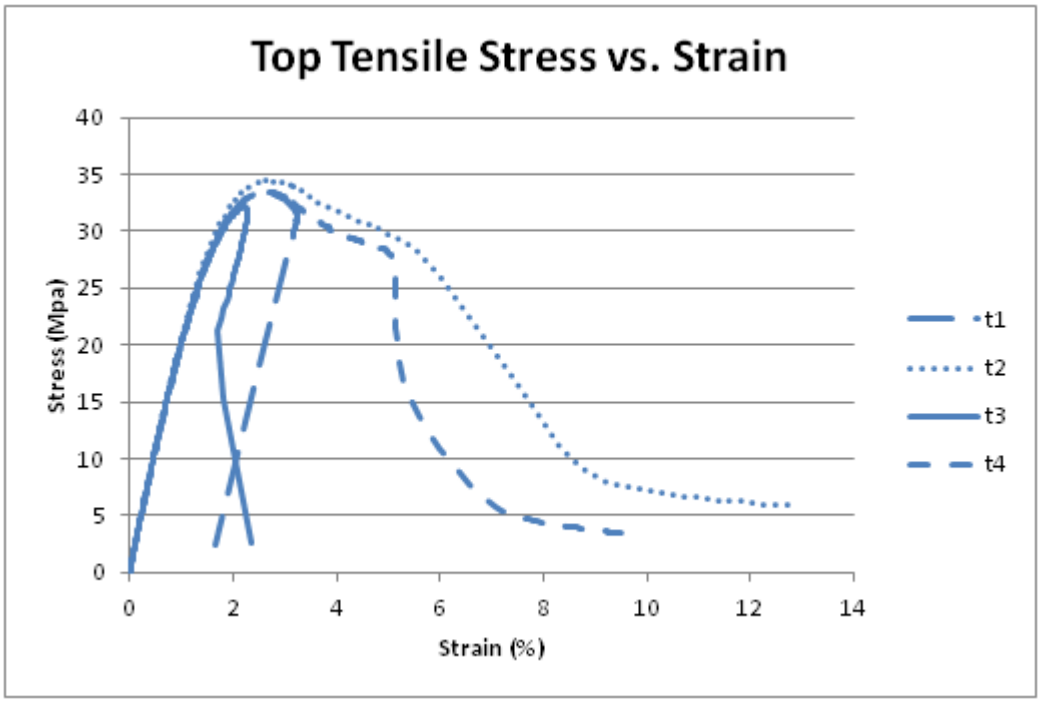

Figure 4.5: The stress versus strain curves for four samples ($t_1 - t_4$) taken from the top of the manifold cover perpendicular to plastic flow during molding as shown in Fig. 4.3.

Occasionally samples such as t_1 and t_3 in Fig. 4.5 appear to have reversed strain at

the end of the testing cycle. These samples had the fracture occur outside the range monitored by extensometer, allowing the extensometer to relax before fracture. This occurred because of the lack of dogbone shaped samples as discussed in Section 4.1.1.

From the stress-strain plot, the tensile yield strength can be determined as the largest stress the sample is able to tolerate before it begins to yield. Once the PVC begins to yield, the apparent stress being measured begins to decrease[16]. The maximum apparent stress value is thus the yield strength of the PVC sample and can be used in comparing the yield strength of the tested PVC samples to the vendor's published strength for the PVC. A comparison of the yield strength of the Rib 3 samples to the samples from the top and sides of the manifold cover will be investigated to see if the PVC across Rib 3 is weaker than the other manifold cover areas.

Samples were taken from the back, top, and front of the manifold cover as shown in Fig. 4.6 and discussed in Section 4.1.1. The top samples, front Rib 3 samples, and back rib samples were all perpendicular to the direction of the flow of the PVC during injection molding while the front and back side samples were parallel to the direction of the flow of PVC.

Since the side samples were parallel to the direction of PVC flow, more of the plastic molecules were aligned along the length of the side samples, and the side samples failed in a ductile manner experiencing significant plastic deformation. The rib and top samples were perpendicular to the direction of PVC flow, so more of the plastic molecules were aligned across the width of the samples instead of the length. This caused the perpendicular samples to fail in a brittle manner with little plastic deformation of the samples before failure. Examples of the two modes of failure can be seen in Fig. 4.7. This alignment of plastic molecules during injection molding should increase the strength of the parallel samples while reducing the strength of perpendicular samples.

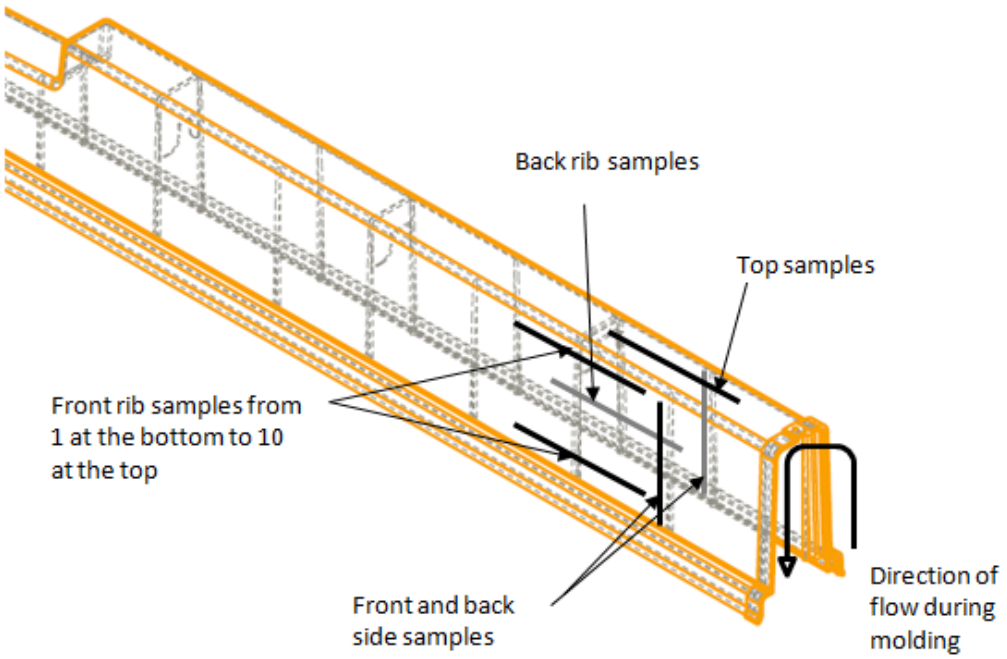

Figure 4.6: The locations on the manifold cover from which the tensile strength test samples were taken. The arrow on the right shows the direction of the PVC flow as the manifold cover was injection molded. The plastic flowed from the back lower edge up across the top then down the front.

Yield Strength Results

The yield strength test results for the rib, top, and side location samples are shown in Fig. 4.8 and listed in Table 4.1. The parallel side samples exhibited a yield strength of 37.2 MPa, about 90% of the vendor's published value of 41.4 MPa[17], while the top and rib samples exhibited a yield strength of 33.4 and 32.7 MPa, respectively, about 80% of the published yield strength.

This slight reduction in measured tensile strength is not surprising as the molding and testing conditions were not as optimal as they would be for the vendor's test. Even so, a significant percentage of the yield strength is still present. Additionally, the parallel

Figure 4.7: The top sample is from the side of the side of the manifold cover and was parallel to the flow of PVC during injection molding. This parallel sample exhibited plastic deformation of the PVC before fracture. The bottom sample was from the top of the manifold cover and was perpendicular to the flow of PVC during injection molding. This perpendicular sample did not exhibit plastic deformation but instead failed by brittle fracture.

side samples were expected to be stronger than the perpendicular top and rib samples due to the alignment of the plastic molecules. The parallel samples were about 10% stronger than the perpendicular samples.

For the most part, the rib did not seem to make a large difference in the tensile strength. Several samples across the rib on both the front and the back of the manifold cover were tested with similar results.

Location (orientation)	**# of Samples**	S_y **(MPa)**	E **(GPa)**
Top (perpendicular)	4	33.4 ± 0.93	2.20 ± 0.054
Rib (perpendicular)	12	32.7 ± 2.0	2.15 ± 0.051
Side (parallel)	4	37.2 ± 1.3	2.40 ± 0.050
Vendor Value[17]		41.4	2.280

Table 4.1: Measured values of the tensile yield strength and modulus of elasticity for each group of samples from the manifold cover.

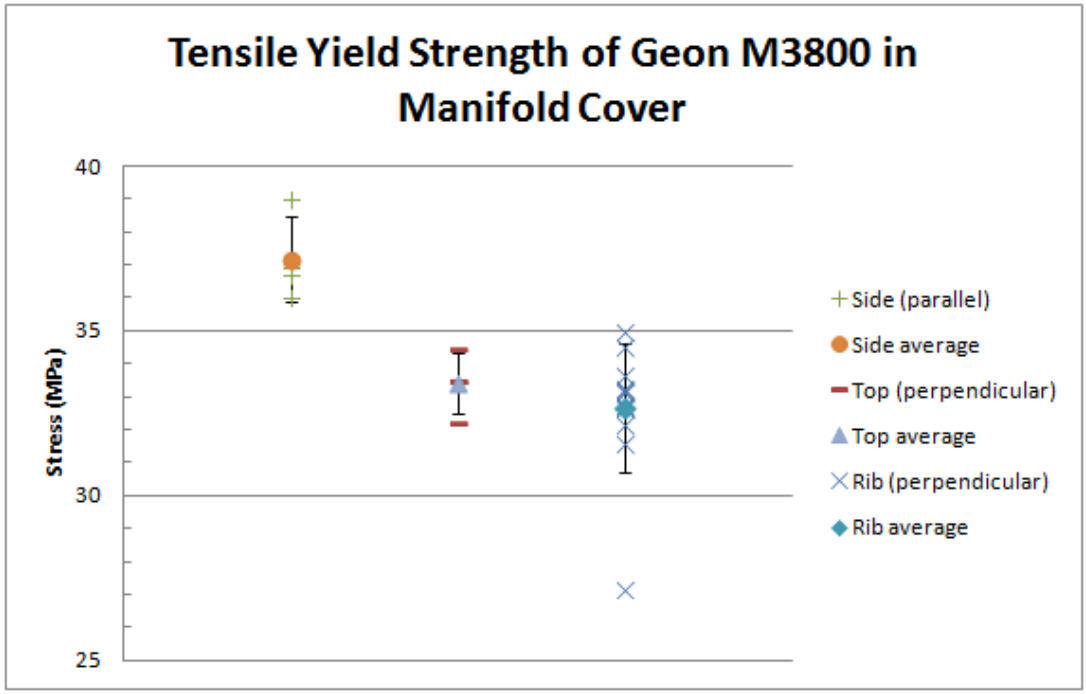

Figure 4.8: Tensile yield strength values for the manifold cover PVC samples. Each individual sample's value is plotted as well as the average with the standard error shown by error bars. The plot range is truncated to allow more detail.

In summary, the yield strength of the side samples was 37.2 ± 1.3 MPa, the yield strength of the top samples was 33.4 ± 0.93 MPa, and the yield strength of samples across the rib was 32.7 ± 2.0 MPa. Thus it appears as if the rib has little effect on the tensile strength compared to the similarly oriented top samples. The yield strength measured was somewhat below the manufacturer's published yield stress of 41.4 MPa for all samples.

Modulus of Elasticity Results

Another comparison of the Rib 3 samples to the other samples is modulus of elasticity which describes the stiffness of a material in the elastic range of loading before plastic

deformation occurs. To determine the elastic modulus of the samples, the linear elastic portion of the stress versus strain plot was fit with a linear regression line. The slope of this line is the elastic modulus of the sample. The linear portion was chosen to be the portion of the curve up to 0.5% strain.

The elastic regime of the samples from Fig. 4.5 are plotted in Fig. 4.9 along with a linear fit of each curve. The slope of the line is the elastic modulus for that sample.

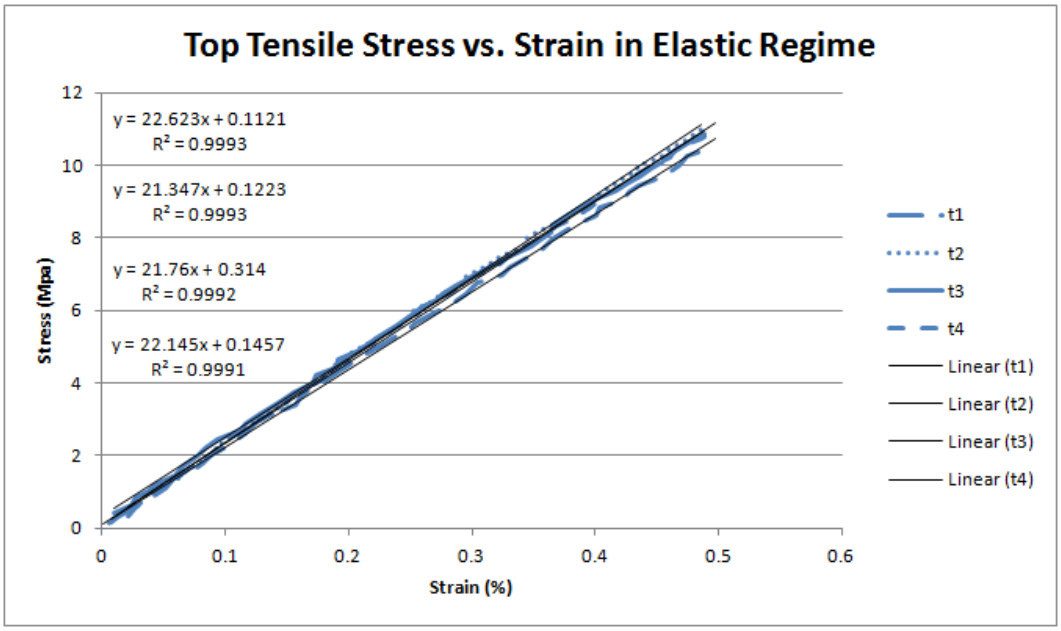

Figure 4.9: This figure displays the elastic portion of the stress versus strain curves for four samples taken from the top of the manifold cover perpendicular to plastic flow during molding whose entire curve can be seen in Fig. 4.5. The linear fit of each series is shown as well as the values of the slopes used to calculate the modulus of elasticity.

The values of the elastic moduli are listed in Table 4.2. It can be seen that the perpendicularly oriented samples had a modulus of elasticity of 2.15-2.20 GPa, about 5% lower than the vendor's published value of 2.280 GPa, while the parallelly oriented samples had a modulus of 2.40 GPa, about 5% higher than the vendor's value. This

Location (orientation)	**# of Samples**	E **(GPa)**
Top (perpendicular)	4	2.20 ± 0.054
Rib (perpendicular)	12	2.15 ± 0.051
Side (parallel)	4	2.40 ± 0.050
Vendor Value[17]		2.280

Table 4.2: Measured values of the modulus of elasticity for each group of samples from the manifold cover.

makes sense as the aligned plastic molecules should add stiffness and strength to the plastic in the parallel orientation. It is also good that the values are close to the vendors's to demonstrate that the injection molding process is not dramatically affecting the physical properties of the PVC.

Strength Across Rib 3

It is of interest to explore whether the rib appears to cause weakness to the tensile samples across it.

Ten samples were tested for tensile strength across Rib 3 on the manifold cover. They were evenly distributed along the front of the manifold cover as described in Fig. 4.6. Sample 1 was taken from near the bottom of the manifold cover where it attaches to the extrusion and the last portion of the manifold cover to fill during injection molding. Sample 10 was at the top of the Rib 3. Samples 8-10 are all on the portion of Rib 3 which has the web used to align the raceways. Only one sample was taken at each location from a new manifold cover.

Figure 4.10 shows the yield strength of the samples across Rib 3. It appears that the web may cause a slight drop in the strength of the manifold cover. Nevertheless, the lowest strength value of 27.2 MPa is still two-thirds that of the data sheet yield stress value of 41.4 MPa. Thus it appears that, while overall the rib does not cause significant strength loss, there may be a weakness in the PVC near the top of Rib 3 close to where

cracks have been observed as discussed in Section 4.3.

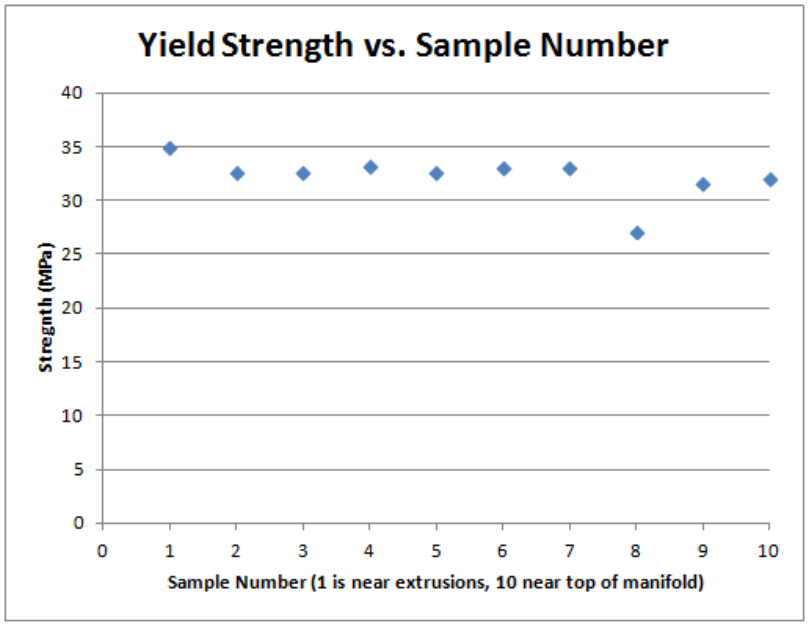

Figure 4.10: The measured yield strength of each sample across Rib 3. Sample 1 is at the bottom of the manifold cover while Sample 10 is near the top of the manifold cover.

Figure 4.11 shows the series of rib samples after testing and demonstrates the location of the failures. In the figure, the samples are pushed together vertically but in reality were actually spaced about 3 mm apart because of the blade width of the chop saw used to cut them apart. Sample 1 is at the bottom of the figure and Sample 10 at the top.

Eight out of ten samples broke at the rib. Samples 5-10 broke on the snout side of the rib while samples 1 and 4 broke on the opposite side of the rib. It is possible that the fracture location is following an injection molding knit line which could switch sides of the rib part way down causing the samples to break on the opposite side of the rib. In injection molding, the knit line is the junction where two fronts of flowing melted plastic come together. As the fronts are exposed to air as they flow, they may cool slightly;

Figure 4.11: The samples across Rib 3 after testing. The location of fracture can be seen for each sample. The ribs are ordered from Sample 1 at the bottom to Sample 10 at the top with Sample 10 obtained from near the top of the manifold cover and Sample 1 from the bottom near the connection with the extrusions.

when the fronts join together, they may not fully melt together thus causing a weakness at the knit. Also this could be from the plastic molecules not being as entangled as in a straight flow.

Samples 2 and 3 broke at a grip in the testing fixturing. This could be because of slight asymmetry in the cutting of the samples, as failure was at the narrower end of the sample.

This test demonstrates that Rib 3 does seem to have some impact on the tensile strength. Some sort of stress concentrator or weakening based on some flaw in the plastic does appear to exist along Rib 3.

4.1.4 Conclusions and Implications

This analysis has shown that the injection molded Geon M3800 PVC used in the manifold covers has a yield strength 80-90% that of the vendor's specification. The PVC is about 10% weaker in the cross flow direction. The PVC samples fail in brittle fracture from cross-flow stress but fail in plastic yielding from with-flow stress. Something may cause weakness on Rib 3, possibly the rib geometry or an injection knit line.

Based in part on results from this section, the new manifold covers will be injected from the top instead of the side to even the PVC distribution and reduce knit lines. Additionally, the mold will be heated to ensure the PVC throughout the part will be well bonded.

4.2 Stress Concentration in Injection Molded PVC

Many parts in the NOνA liquid scintillator detector are made out of either extruded or injection molded PVC plastic. Plastic under any stress is susceptible to creep and eventually failure if the stress is great enough. Certain geometric features such as sharp concave corners can cause concentration of stress which can cause failure at those locations even when the overall stress on the part is low.

It was desired to find how sensitive the plastic used in the detector is to stress concentrators and how increasing the fillet radii in certain areas would lower the stress. Since the most significant stress seen by the parts is bending stress, the experiment to test the stress concentration used bending stress caused by a cantilevered load.

Tests were performed on L-shaped injection molded PVC samples with a force applied to one end of the L as a cantilever imposing a calculated bending stress on the corner of the L. The test fixture is shown in Fig. 4.12. The time between the loading of the stress and the failure of the part was recorded by a webcam capturing a series of

images.

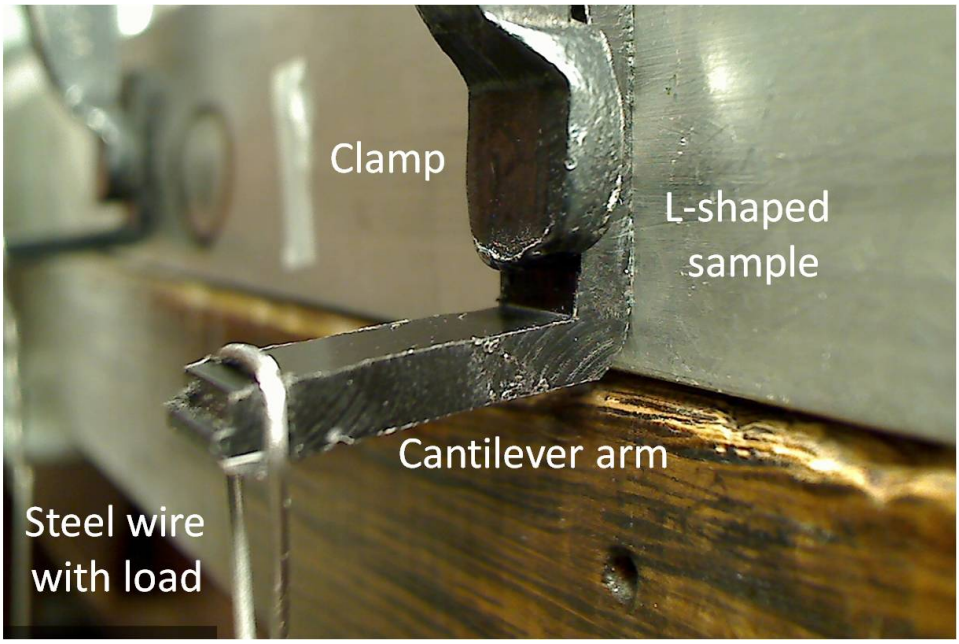

Figure 4.12: The stress concentration test set up. The upright of an L-shaped PVC sample from the snout back is clamped firmly in place while a force is applied by a weight hanging from steel wire at a specific location on the cantilevered arm of the sample.

Tests looking at three different aspects of the PVC cracking were performed. The first compared various fillet radii to investigate the sensitivity of the initial variety of PVC used in the detector, Geon M3800, to various levels of stress concentrations. The second test compared a second, stronger PVC variety, Geon M3500 PVC, to the originally used Geon M3800 to see if a different PVC was preferable. The final test examined the relationship between the level of stress applied and the time until fracture occurred for Geon M3800 PVC of a consistent fillet radius.

The results of these experiments assisted in determining how stress could be reduced in the snout and manifold design as well as the selection of a PVC of appropriate

strength.

In this chapter, Section 4.2.1 describes the test set up in more detail. Section 4.2.2 explains the process of performing the tests.

Section 4.2.3 presents the results, including the effect of corner radii, the effect of changing PVC resins, and the behavior of the M3800 resin at different levels of stress.

4.2.1 Set Up

Section 4.2.1 explains how the testing apparatus was assembled. Section 4.2.1 describes the preparation of samples from the snout back into L-shaped cantilever samples.

Experiment Fixture Set Up

In order to create a bending stress at the corner of the sample, one arm of the sample was clamped while a load was hung from the other arm. The unbent arm was aligned vertically to allow the load to be applied perpendicularly to the other arm using gravity. To do this, a piece of angle iron was clamped to the work bench and the samples clamped to the angle iron. When several samples were tested concurrently, a square rod was used to clamp the samples all at once with several clamps distributed along the length of the rod as shown in Fig. 4.13. When only one sample was tested, a c-clamp held the sample directly to the angle iron to allow the camera to view the corner of interest as shown in Fig. 4.12.

To achieve the desired bending moments, weights were hung from the sample's cantilever arm. The samples were positioned with enough space between them to prevent the weights from interfering with each other during testing. The length of the wires on the weights allowed the weights to rest on a block before testing began to allow synchronized application of the stress. Enough clearance was given to allow full fracture of the test samples without the weights touching the floor.

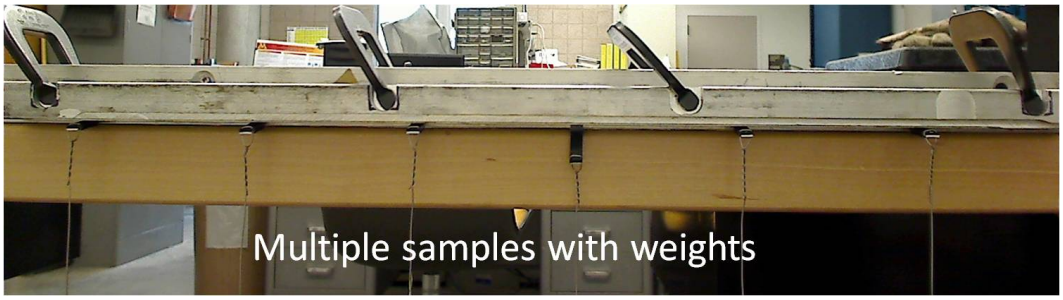

Figure 4.13: The stress concentration test set up for multiple samples. Multiple samples are clamped in place with a square rod.

Data were recorded in the form of time-stamped images taken with a high resolution webcam at specified intervals. The camera was positioned at the same height level as the samples in a manner able to observe six samples concurrently and far enough away to minimize distortion. The camera used was a Logitech 9000 webcam with manual focus which took still shots at 1920x1000 pixel resolution. A free software application called Yawcam was used to control the camera and the frequency of the image captures [18]. These images were saved onto an external USB hard drive.

Lighting was provided by a 60W desk lamp positioned to minimize glare and shadows and ensure uniform lighting for samples, especially those used in experiments lasting several days.

Sample preparation

Samples were obtained from the back snout half. The snout attaches to the open end of the manifold cover and contains the optical fibers as they exit the cells through the manifold cover (see Fig. 1.3). The snout was not designed to be under stress but to be light- and air-tight. Thus, in the design at time of testing, a sharp corner was present on the junction of the top and side of the snout half. On technical drawings, this corner

had a radius of zero, and the injection molded part was assumed to also have a radius of zero. Later, this fillet radius was increased by grinding down the edge on the die to reduce this potential stress concentrator. The radius appears to be about 0.5 mm as measured with calipers by eye.

A two step process was used to cut out the samples. First, the rough shape of the L-shaped samples was cut out with a band saw from the original snout half as shown in Fig. 4.14. Each of these pieces was about 10 mm wide while the desired final width was 6 mm.

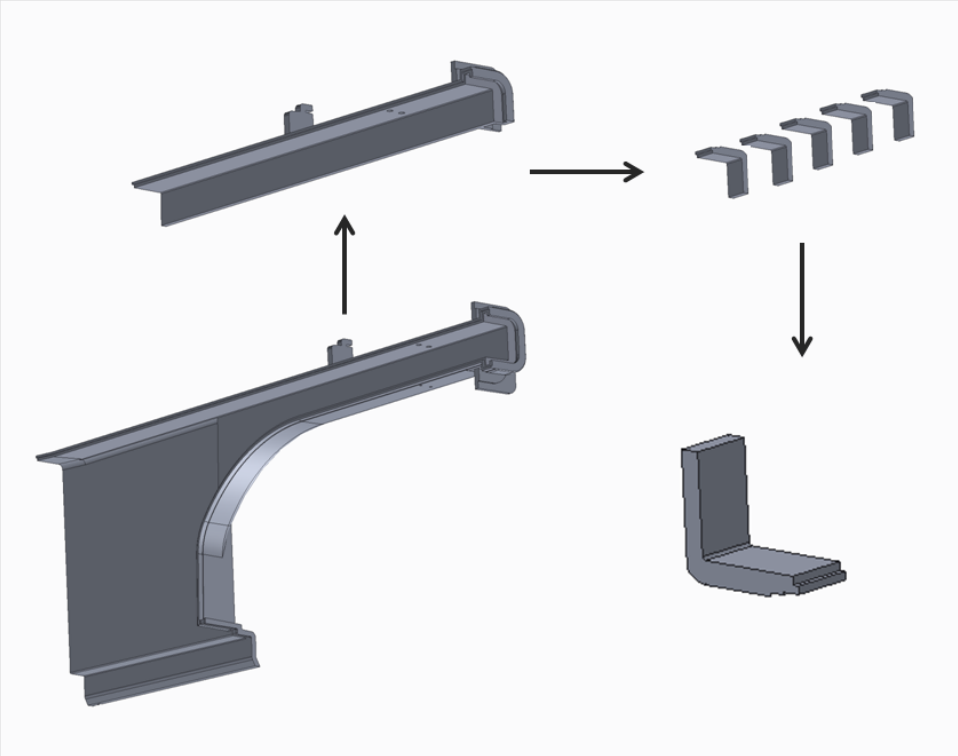

Figure 4.14: A snout back from which sample were obtained. The rough shape of the samples was cut out with a band saw and later milled to final width and smoothness.

The second step involved using an end mill to reduce the sample width from 10

mm to 6 mm. Samples were nested and clamped with wooden forms during the milling process as shown in Fig. 4.15. As the compression of the samples occasionally caused the samples pressed by the pointed clamp half to begin to crack at the joint, only samples nested in the concave clamp half were used, and top samples were discarded. Each sample was carefully examined afterward to see if any signs of stress were present.

Figure 4.15: A model of the clamp fixture used to mill the L-shaped samples. Five sample pieces were nested and held in place between two wooden forms. Sample geometry is shown modified for clarity; the inside corner radius has a maximum value of approximately 0.5 mm in the actual specimens.

After milling, the edges of the samples were deburred carefully. Notches were cut into the sides of each sample to keep the weight support wire in the proper place.

4.2.2 Test Procedure

To begin an experiment, any remaining flashing from the milling preparation was removed from selected samples with a sharp knife. Care was taken to avoid damaging the

inner corner of the sample. The samples were then clamped to the fixturing as discussed in above in Section 4.2.1.

The width and thickness of each sample was measured with a micrometer, and the force corresponding to the desired stress was calculated. A weight was then made to match this needed force from a bottle and steel shot. Steel wire was used to hang the weights from the cantilever arm of the sample. Each hanging mass was weighed with its hanging wire in order to achieve an accurate result.

In order to achieve simultaneous zero-time on all samples in an experiment, each hanging mass was attached to its sample and rested on a block. After the camera had been started, the block was removed. Any swinging of the weights was eliminated to keep the stress constant on the samples.

A webcam was used to record still images of each sample at regular intervals. The camera was controlled with a computer which set the rate of image capture. The computer also controlled the focus of the camera as well as brightness and contrast of the images. Each image was stored with the timestamp as part of the file name, as well as watermarked on the image, to allow easy evaluation of data.

After obtaining the images, the images were examined to determine the time when each sample failed.

4.2.3 Results

The goal of these experiments was to gather information about Geon M3800 PVC, the original choice for the manifold covers, snouts, and end and side seals. The sensitivity to stress concentrators of the M3800 was examined as well as the nature of its failure under various levels of bending stress. Additionally, a stronger and tougher formulation of PVC in the same series, M3500, was compared to the M3800.

Three experiments were performed, and the results are reported below. First, the

effects of different corner radii on M3800 samples is explored. Second, the notch sensitivity of M3800 is compared with that of M3500 resin. Finally, the behavior of M3800 resin under different levels of imparted stress is examined.

Stress Concentration of M3800 of Differing Radii

Geon M3800 PVC was originally used for the snout and manifold cover as well as several other parts in the liquid scintillator detector construction. It was desired to know how sensitive this PVC is to increased stresses due to stress concentrators such as small radii on internal corners.

In this experiment, the L-shaped samples prepared in Section 4.2.1 were tested. This experiment compared the failure time of the zero fillet radius samples to those with an added fillet radius of about 0.5 mm.

Samples were tested in the manner described in Section 4.2.2. The test was run with a bending stress at the sharp corner, unmodified to account for stress concentration, of 29.0 MPa, seventy percent of the vendor's published yield stress of 41.4 MPa. Three samples with a corner radius of 0.0 mm were tested; five samples with a corner radius of 0.5 mm were tested.

Figure 4.16 shows observed failure times of the two sets of samples. Although the larger radius samples do appear to have taken slightly longer to fail than the smaller radius samples as expected, as well as having the longest times, there is a great amount of scatter in the times from both sample sets and the observed difference between the two groups is not statistically significant. It could be that some of the samples used had defects which caused early failures. The quality of the samples may have been too low for the sensitivity of the experiment.

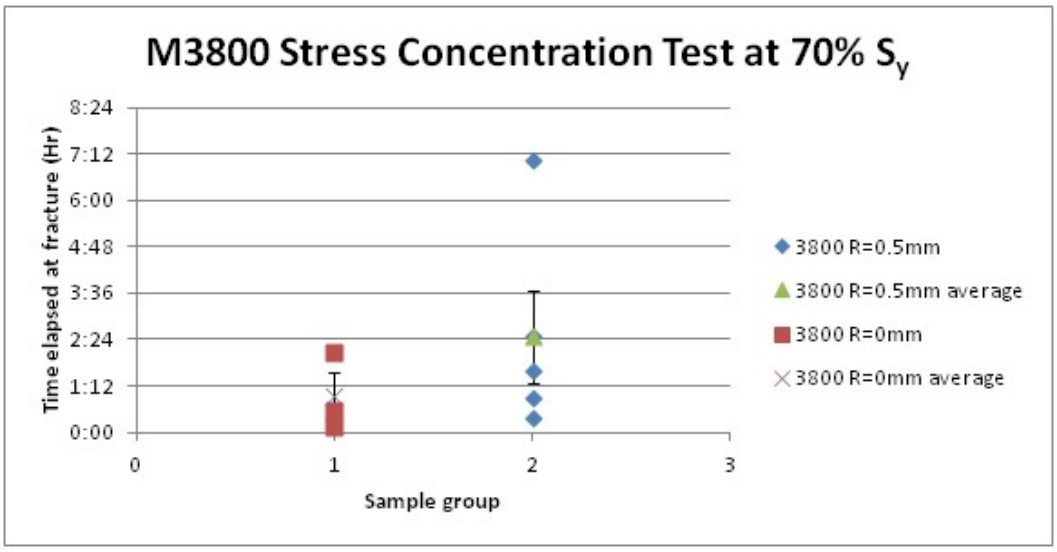

Figure 4.16: The results of the stress concentration experiment for varying corner radii. The squares on the left show the time elapsed from stress application to failure for the samples with a radius of 0 mm. The diamonds on the right show the elapsed time for the samples with a radius of 0.5 mm. The mean with standard error bars are also shown for both sample sets.

Stress Concentration Comparison of M3800 vs. M3500

It was considered that the Geon M3800 may not be strong enough if the snout needs to be load bearing. It was desired to test a stronger and tougher PVC in the same product line as the M3800, which has a tensile yield strength of 41.4 MPa and an elongation at fracture of 35%. The PVC Geon M3500 was chosen as it has a tensile yield strength of 46.2 MPa and elongation at fracture of 50%. This test intended to examine if the M3500 is more tough and crack resistant than the M3800.

All samples were tested at the same nominal stress of 29 MPa, which is 70% of the yield strength of the M3800 and 63% of the published M3500 yield strength[19]. While M3500 has higher published strength and strain at fracture, it also is more viscous and thus is not as easily injection molded. This is a concern as some of the parts are thin

and difficult to mold.

As can be seen in Figure 4.17, the M3500 has a much longer time until failure than the M3500.

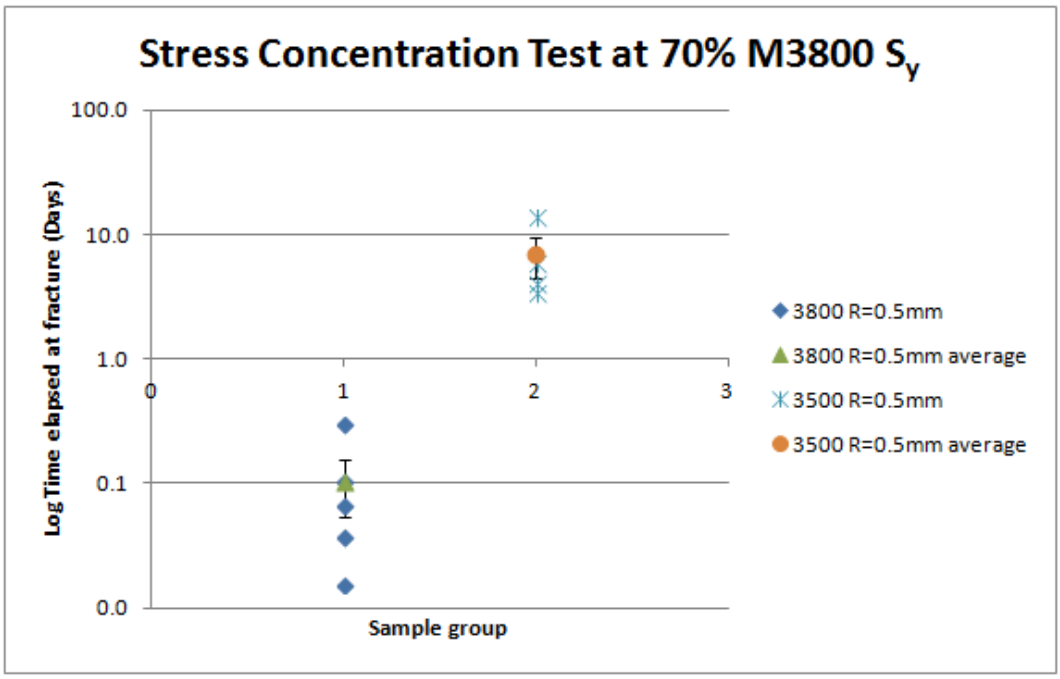

Figure 4.17: The time until failure of the stress concentration experiment for two different injection molded PVC varieties. The diamond set on the left shows the time elapsed from stress application to failure for the samples made of Geon M3800 PVC. The cross set on the right show the elapsed time for the samples made of Geon M3500 PVC. The mean with standard error bars are also shown for both sample sets. The time axis is plotted on a log scale.

The M3500 PVC is clearly much stronger than the M3800 as it takes days instead of hours for the M3500 samples to fail. The M3500 took 166 $\pm$ 58 hours to fail while the M3800 took 2.5 $\pm$ 1.2 hours to fail.

This experiment used four M3500 samples and five M3800 samples. Although both groups exhibited substantial scatter, the results are two orders of magnitude different

and thus very statistically significant.

For M3500 to even be considered, it must not interact with the pseudocumene in the detector. Chapter 3 discusses the process of testing interaction. The M3500 did not indicate any interaction with the detector scintillator and thus is acceptable for use in the detector.

Thus it appears that M3500 is a better choice to help prevent cracking in the snout and manifold cover.

Varying Levels of Stress on M3800

The third experiment looked at the failure behavior of M3800 under various stresses. For this experiment, at each stress level, a single sample was observed for the duration of its life. Instead of merely observing it from a head on perspective as shown in Fig. 4.13, for this experiment the sample was observed from the side as shown in Fig. 4.12. The camera was placed as close as possible to the joint in order to capture the entire process of failure. This distance was limited by the focal range of the camera which has a minimum focal length of 2.5 cm. Images were then recorded for the duration of the sample's life. These images can be inserted in series into a movie clip to show the rate and nature of the failure.

Each sample was lit with a desk lamp and the setup covered with a black cloth to moderate the lighting as much as possible. For the samples that took several days to fail, slight lighting differences occurred between day and night but the detail of the sample can still be seen.

It was of interest to observe how the sample failed at various stresses. Several different times during the failure were notable. These included when the first stress whitening can be seen on the sample, when the sample begins to fail rapidly, and when the sample fails completely. Tests were performed for 40%, 50%, 60%, 70%, and 80%

of the 41.4 MPa yield stress of the M3800 with the minimal corner fillet radius. One sample was tested per stress level. The results are listed in Table 4.3 and discussed below.

% yeild stress	*40%*	*50%*	*60%*	*70%*	*80%*
force applied	0.0	0.0	0.0	0.0	0.0
crazing observed	516.4	72.85	0.225	0.137	1.34
start break	533.6	75.61	0.837	0.809	1.35
end break	534.8	75.63	0.866	0.816	1.36
Percent total time from crazing to failure	3.4%	3.7%	74%	83%	1.5%
Percent total time in fast failure mode	0.22%	0.04%	3.30%	0.85%	0.78%

Table 4.3: The times in hours after applied load that each sample was observed to exhibit various phases of failure.

It is observed that generally as the stress decreases, the time until fracture increases as one would expect. Generally, the sample bends very slowly for the majority of its duration and then bends and breaks relatively rapidly near the conclusion of its life.

Table 4.3 lists three time measurements for each sample all measured in hours from the time the bending force is applied to each sample. Figure 4.18 pictures examples of each of the notable times. The third row indicates when crazing marks are observed on the surface of the sample. These crazing marks offer some indication that the stress level is causing some damage to the sample and that the sample is beginning to fail. After the initial displacement caused by the application of the weight on the sample, the sample generally bends very little until after crazing is observed. Once the sample begins to fail, the rate of deflection increases significantly and the sample fails quickly. The fourth row in the table gives the time when the sample begins to deflect more quickly. This indicates when the sample is close to complete failure as creep transforms into failure. The fifth row reports the time the sample fails catastrophically.

The sixth row of Table 4.3 lists the percentage of total breaking time that occurred

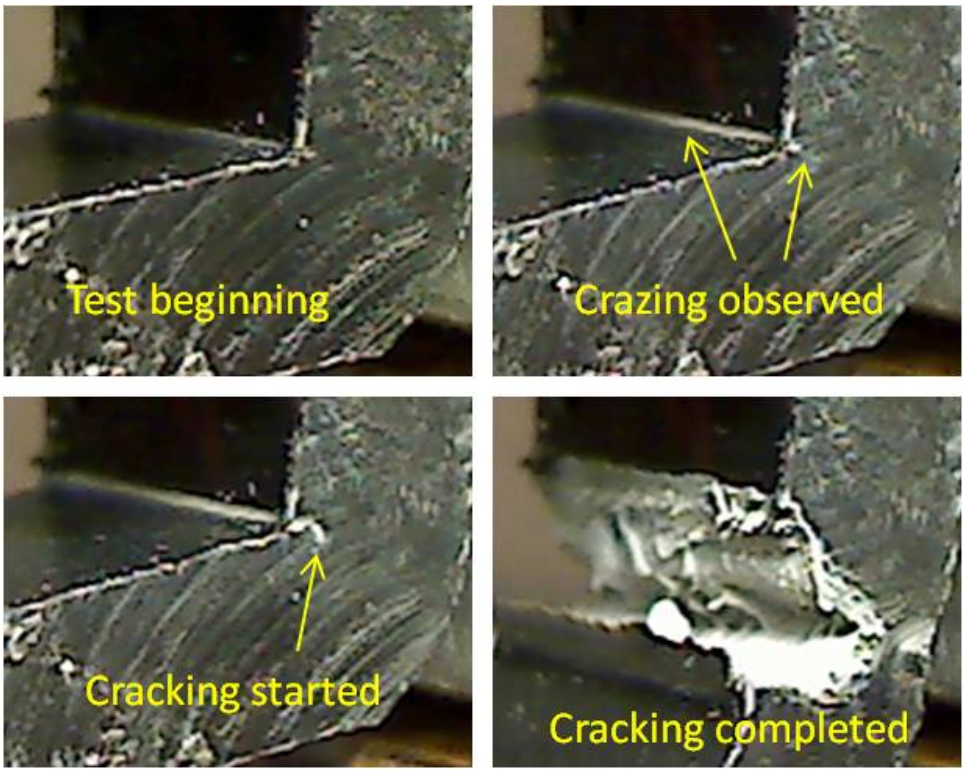

Figure 4.18: The sample at four stages of failure. The upper left panel shows the sample immediately after the load was applied. The upper right panel shows when crazing is just beginning at the corner feature. The lower left panel shows the sample beginning to break. The lower right panel shows the sample after catastrophic failure occurs.

after crazing is observed on the surface of the sample. The seventh row indicates for how much of the total breaking time the fast failure mode occurs.

Figure 4.19 shows on a semi-log plot the various times described in Table 4.3. As expected, failure times generally increase as the applied bending force decreases. This holds especially true for the 40% and 50% S_y samples. The 60 and 70% samples do appear to experience failure differently than the 40, 50, and 80% samples. The 60 and 70% samples fail sooner than the 80% sample which was unexpected as they have a lower applied stress level. Additionally, the crazing is observed much more quickly into

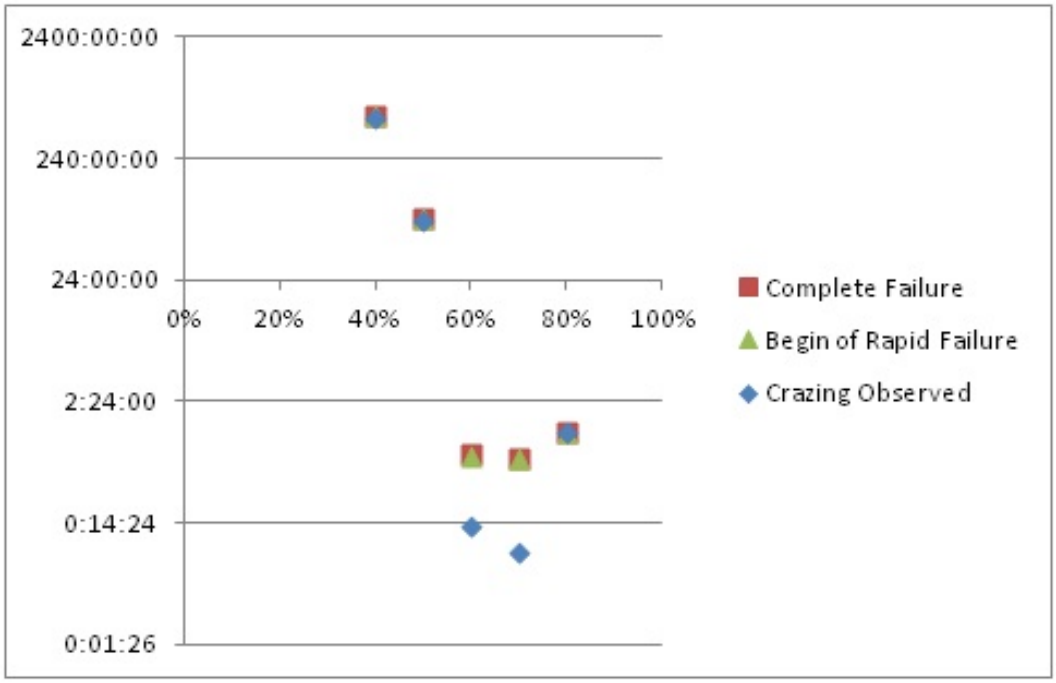

Figure 4.19: The time crazing is observed, rapid failure begins, and complete failure occurs for M3800 zero radius samples with applied stresses from 40% S_y to 80% S_y plotted on a log scale.

the lifetime of the the 60 and 70% than the others. This indicates that there may be some inherent difference in the particular samples.

It is difficult to prove a trend with only one sample at each stress level. While information about the nature of M3800 can be gleaned from these tests, the statistics are not robust enough to establish definite trends.

It is interesting to note the appearance of the fracture for the various levels of applied stress. Figure 4.20 shows an image of each sample after failure. It can be seen that the lower stress level samples demonstrate a relatively clean fracture with minimal hairiness on the cleavage surface, while the higher stress level samples show much more entanglement of the plastic molecules during fracture.

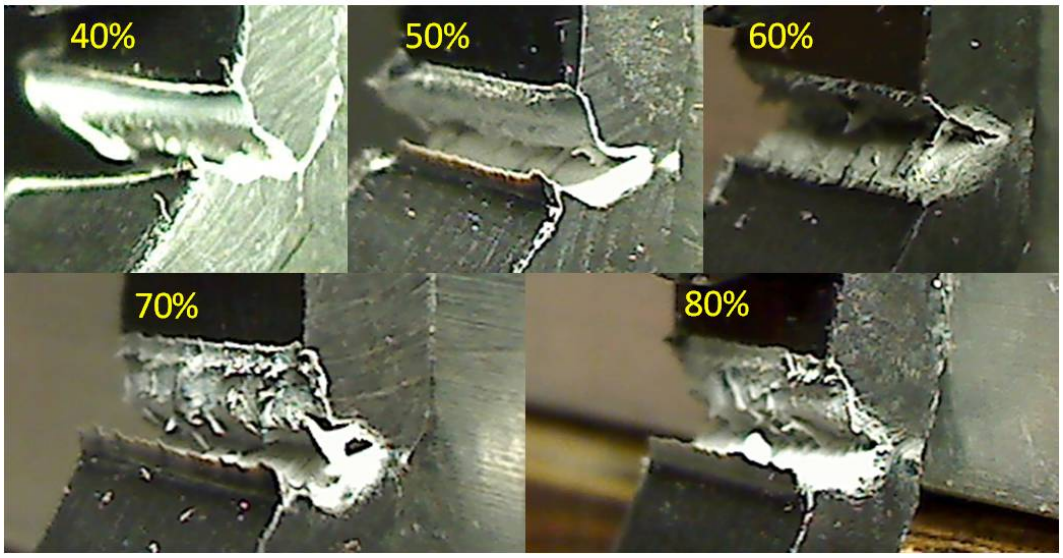

Figure 4.20: The samples of various applied stresses after catastrophic failure has occurred.

4.2.4 Implications and Conclusions

The purpose of the experiments in this Section was to discover general trends in the failure of PVC samples cut from snouts when involving a natural stress concentrator such as a filleted corner. Although it was observed that the fillet radius seemed to make a slight difference in the rapidity of failure, decreasing the applied stress, in general, appears to exponentially increase the time until failure. Additionally, using M3500, a PVC with a yield stress about 10% greater than the originally used M3800, increased the time until failure by two orders of magnitude.

To incorporate these results into the detector design in order to mitigate the risk of future cracking, the manifold cover was redesigned to minimize possible stress concentrators by eliminating the ejector pins and webs to hold the raceways and by increasing fillet radii. Geon M3500 PVC was used to mold the manifold covers and snouts as it was

much stronger and more resistant to cracking than the previously used Geon M3800. Additionally, the overall stress on the manifold covers and snouts was reduced by lowering the pressure applied during the pressure test and improving the containment units used in the pressure test as discussed in Section 4.3.2.

In light of the results found in this section, further work could be done. Straight samples could be tested to determine the bending strength and failure behavior of the PVC without a corner fillet stress concentrator. Additionally, more tests could be performed to improve statistics, especially in the long term stress concentration tests described in Section 4.2.3. Finally, an improved method of fabricating samples could be developed to reduce the scatter in the results in Section 4.2.3.

4.3 PVC Crack Initiation and Propagation

After near detector modules were assembled into blocks for use in the near detector, the manifold covers in several near detector modules were found to have developed cracks. The cracks progressed through the PVC on the manifold covers at the third rib on the side opposite plastic injection. It was desired to find the extent of the cracking as well as potential causes and solutions.

Section 4.3.1 details an initial study to determine the frequency of cracking in manifold covers from modules pressure tested at 1.4 bar. Cracks were discovered in ten out of sixteen manifold covers pressure tested at 1.4 bar.

Section 4.3.2 describes a study of manifold covers tested at lower pressures of 1.0 and 0.7 bar to determine acceptable testing pressures. No cracks were found in nineteen manifold covers tested at 0.7 bar, and one out of ten manifold covers tested at 1.0 bar had a crack at the web-rib interface.

Finally, Section 4.3.4 describes a study using a polarizer to differentiate between reflections and stress marks on the web-rib interface. While some stress marks are found

at all test pressures, including new manifold covers, they do not appear to indicate the initiation of cracking.

4.3.1 Study of Cracks on Inside of 1.4 bar (20 psi) Tested Manifold Covers at Rib 3

After cracks were discovered through the manifold covers on several modules which had been assembled into blocks, it was additionally found that there were cracks on the inside of manifold covers that had been pressure tested but not yet assembled into blocks. It was desired to find how many manifold covers had cracks introduced through the process of being built into modules, presumably from the pressure testing.

To perform the study, twenty-one manifold covers which had undergone pressure testing at 1.4 bar (20 psi) were dissected. These manifold covers were from modules in the sick bay, a group of modules which failed inspection in some way and were deemed unfit for the detector. The manifold covers examined in this report had undergone pressure testing but were placed in the sick bay for reasons unrelated to pressure testing. For each of these modules, the portion of the manifold cover surrounding the third ejector pin boss was removed from the manifold cover and examined for cracks.

The primary locations where cracking was observed was located on the seam between Rib 3 and the manifold cover surface as well as at the interface where the end of the webbing meets the rib. These locations are pointed out in Fig. 4.21.

Five of the manifold covers were from early modules where the webbing connecting the ejector pin ribs between the front and back of the manifold cover had been completely or partially removed to allow the raceways to fit during module production, as shown in Fig. 4.22. Of these five, one had a slight crack while the remaining four had no cracks.

Sixteen of the manifolds had the webbing intact. Six of these manifolds had no indication of internal cracks at Rib 3. The remaining ten all had cracks on the interface

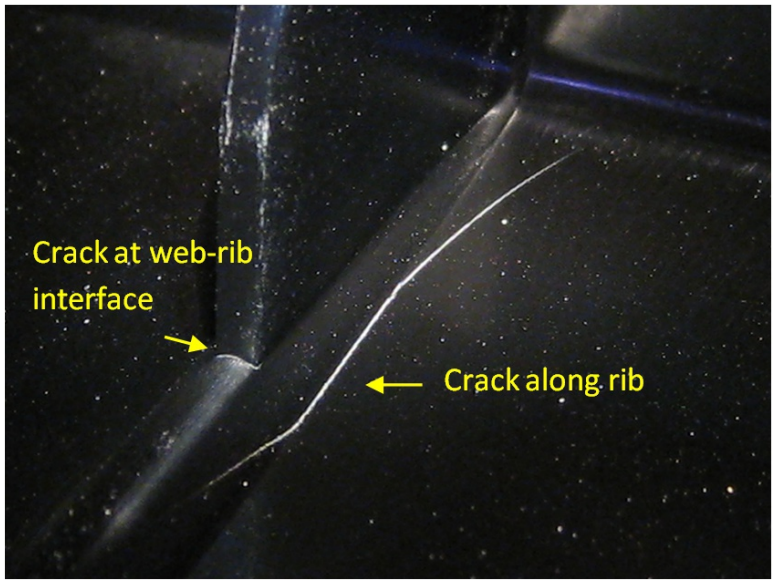

Figure 4.21: Crack at Rib 3 in 1.4 bar (20 psi) old containment tested manifold cover demonstrating a crack along the rib and a crack at the web-rib interface.

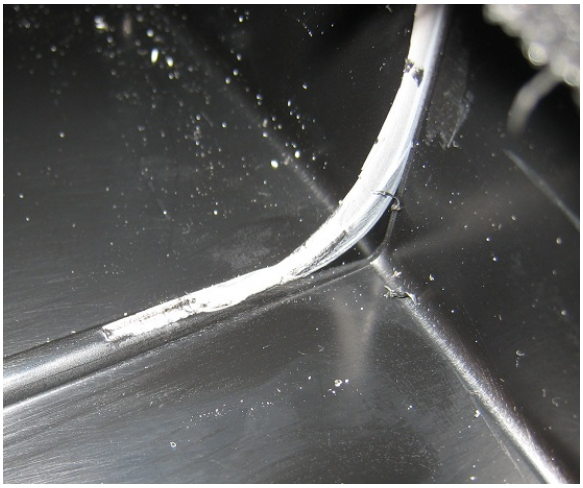

Figure 4.22: The removed webbing from Rib 3 of the manifold cover.

between the rib and the manifold cover inner surface. The cracks had varying degrees of severity.

All ten of the manifold covers had cracks on the side of Rib 3 opposite the snout which is where through-cracks were observed in the IPND. One manifold cover had an additional crack on the snout-side of Rib 3.

The smallest cracks were about a centimeter long and occurred on the seam between the ejector pin rib and the inner surface of the manifold cover. These cracks are located along the rib where the webbing on the top of the rib ends, as shown in Fig. 4.23. Three of this crack variety were found. One of these also had a shorter crack on the snout side of Rib 3 as well.

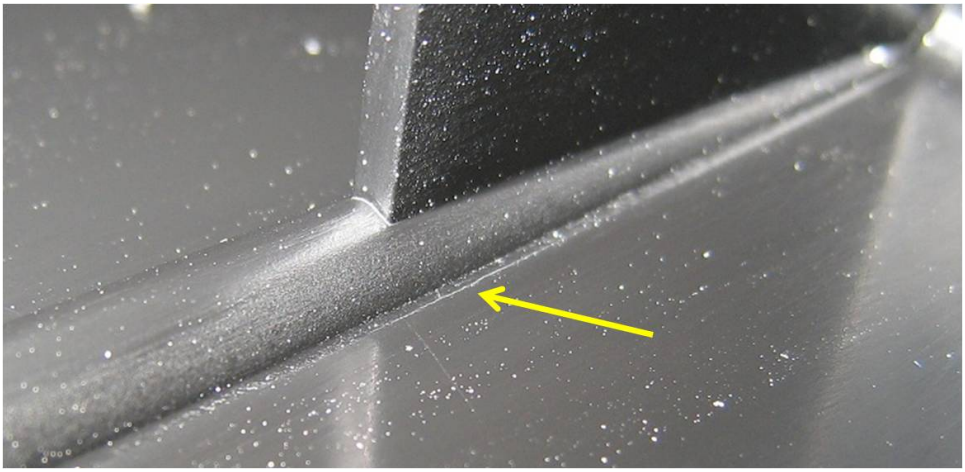

Figure 4.23: A small crack occurring on the interface between Rib 3 and the inside surface of the manifold cover.

Slightly larger than the previous, the middle-size cracks extend further along the rib-surface seam and begin to crack up onto the rib below the end of the webbing, as shown in Fig. 4.24. Of this type, four were found.

In addition to cracking up onto the rib, some cracks also expand outward onto the

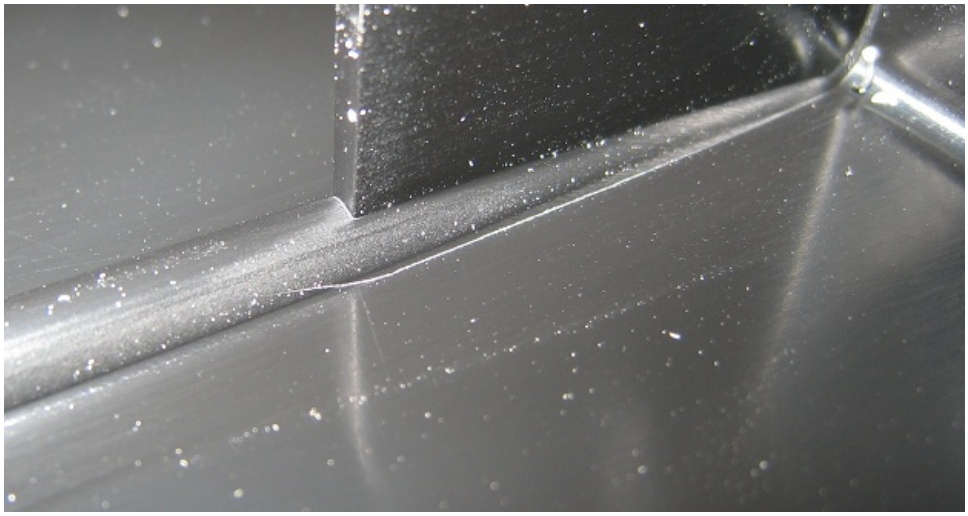

Figure 4.24: A medium sized crack occurring on the interface between Rib 3 and the inside surface of the manifold cover and progressing up onto Rib 3.

main surface of the manifold cover and upward toward the top of the manifold cover, as shown in Fig. 4.25. Two cracks of this type were found.

One manifold cover was found to have cracked at the webbing down to the surface of the manifold cover as shown in Fig. 4.26. This manifold cover also had the second crack variety discussed above and shown in Fig. 4.24.

For horizontal module manifold covers, seven had cracks and three had no cracks. For vertical module manifold covers, three had cracks and three had no cracks.

4.3.2 Study of Internal Cracks on 1.0 and 0.7 bar (15 and 10 psi) Pressure Tested Manifold Covers

After cracks were found along Rib 3 for a large proportion of 1.4 bar (20 psi) pressure-tested manifold covers as detailed in Section 4.3.1, it was desired to determine what pressures are acceptable for pressure testing modules that have the original manifold

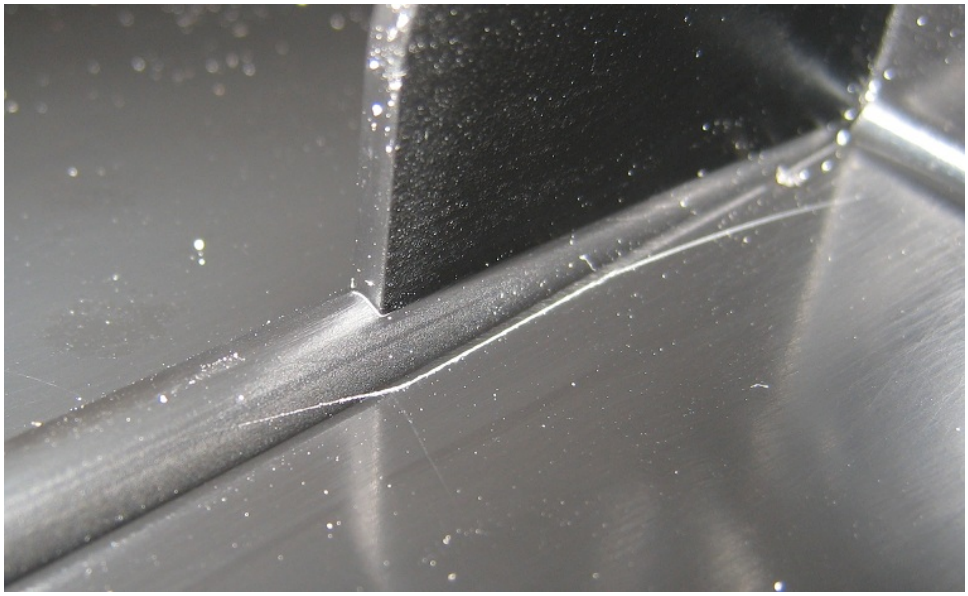

Figure 4.25: A large crack occurring on the interface between Rib 3 and the inside surface of the manifold cover. The crack continues up the curvature of Rib 3 on the lower end while progressing out into the surface of the manifold cover away from the rib on the upper end.

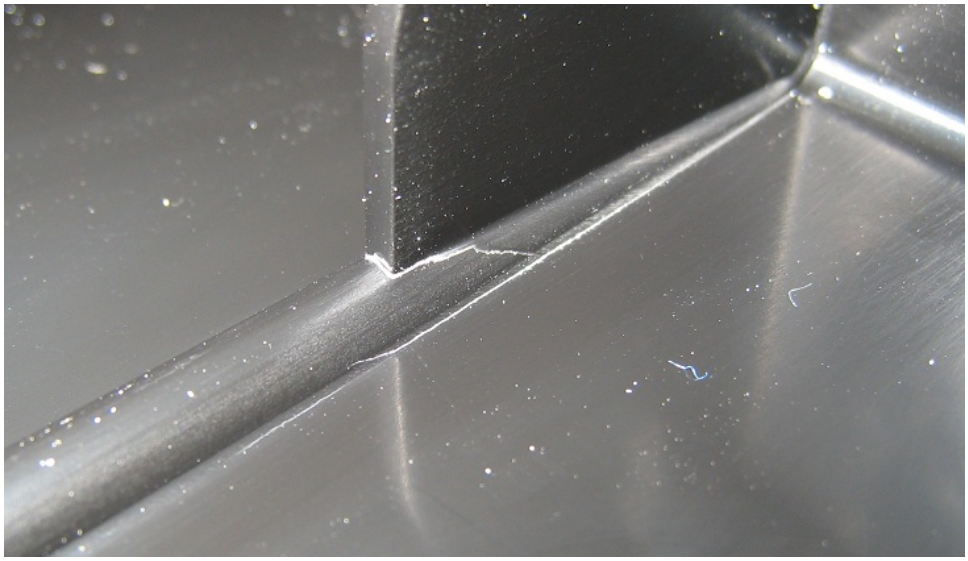

Figure 4.26: A large crack occurring on the interface between Rib 3 and the inside surface of the manifold cover. A second crack can be seen starting at the web-rib interface and progressing down to the crack along the rib.

cover design while avoiding the formation of cracks on the inside surface of the manifold cover. An immediate alteration to the pressure test was increasing the support of the containment units used in the test. Manifold covers were then tested to see if reducing the test pressure from 1.4 bar to 1.0 or 0.7 bar would minimize the formation of cracks.

During the pressure test, containment units are placed on the manifold covers to prevent them from expanding and breaking under pressure. The containment units are 13 mm plates of aluminum sandwiched onto the sides of the manifold cover with aluminum supports holding the two plates in place. The original containment units had five supports spaced evenly along the length of the manifold cover. A model of the original containment unit is shown in Fig. 4.27. These original containment units were used in the pressure tests of the manifold covers described in Section 4.3.1 which were tested at 1.4 bar (20 psi). When pressurized, the manifold cover pushed the aluminum plates, and the plates bowed outward between the supports.

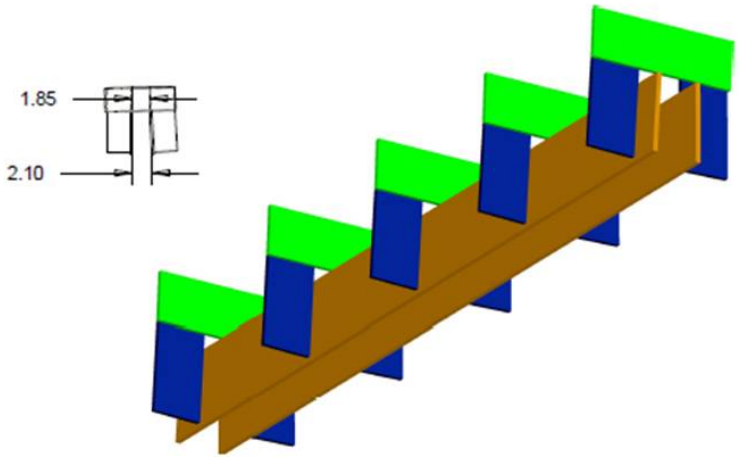

Figure 4.27: A model of the original pressure test containment unit with five supporting cross members.[20]

After cracks were discovered in the manifold covers, the containment units were

stiffened by adding more braces to reduce by half the distance between braces. The new containment units added four more supports in between the original supports thereby reducing the deflection of and stress in the manifold cover during testing. A comparison photo of the old and new containment units is provided in Fig. 4.28.

Figure 4.28: A comparison of the old and new containment units for the pressure test. Shown on top, the old containment unit has five supports while, on the bottom, the new containment unit has nine supports.[20]

Nine manifold covers were pressure tested at each of 1.0 and 0.7 bar (15 and 10 psi) using the new containment units. Using the old containment units, ten manifold covers were pressure tested at 0.7 bar (10 psi). All ribs were then examined for cracks. Ribs 3, 5, and 7 were of particular interest as they had an additional webbing across the width of the manifold cover. The locations of these ribs are labeled in Fig. 4.29 and pictures of the web-rib interface for each rib shown in detail in Fig. 4.30.

Because the reflection due to the small fillet radius at the web-rib interface appears similar to a stress mark as seen in Fig. 4.30, Section 4.3.4 details the process of determining if a stress mark does exist.

At manifold covers tested at pressures less than 1.4 bar, no cracks along the rib were

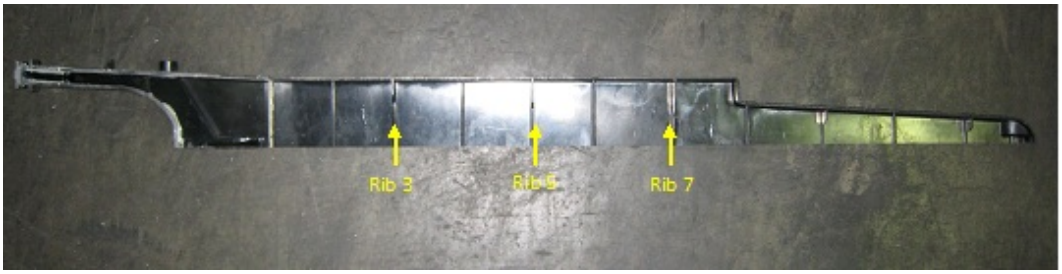

Figure 4.29: Cross section of manifold cover section with Ribs 3, 5, and 7 labeled.

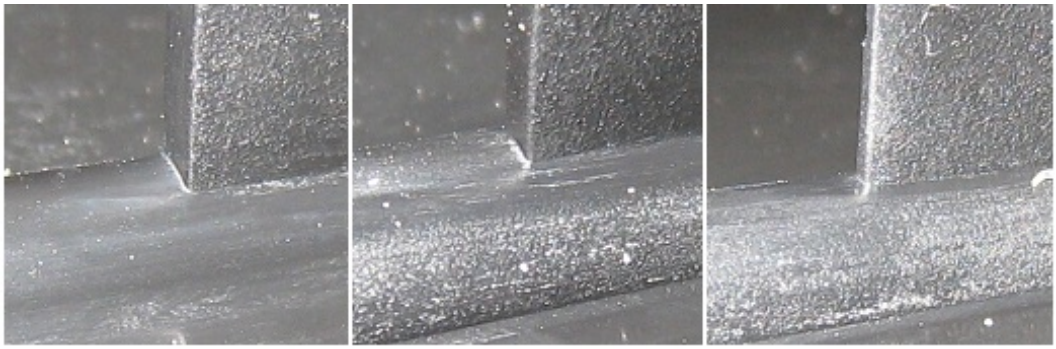

Figure 4.30: New manifold cover Ribs 3, 5, and 7, from left to right, at the interface between the webbing and the rib.

observed. In one manifold cover tested at 1.0 bar, a very small crack was observed at the web-rib interface. There were no cracks parallel to the ribs on the interface between the ribs and the inner manifold cover surface, as was the case in 10 out of 16 at Rib 3 in 1.4 bar-tested manifold covers.

Nine manifold covers which had been pressure tested at 1.0 bar (15 psi) for 20 hours with new containment units were examined. One manifold cover had a crack opening up at the web-rib interface of Rib 3 and progressing a couple millimeters underneath the web as shown in Fig. 4.31. Two others had increased whitening at the web-rib interface at Rib 3 but did not appear to have a crack. One manifold cover had a possible initiation of a crack at the web-rib interface of Rib 7.

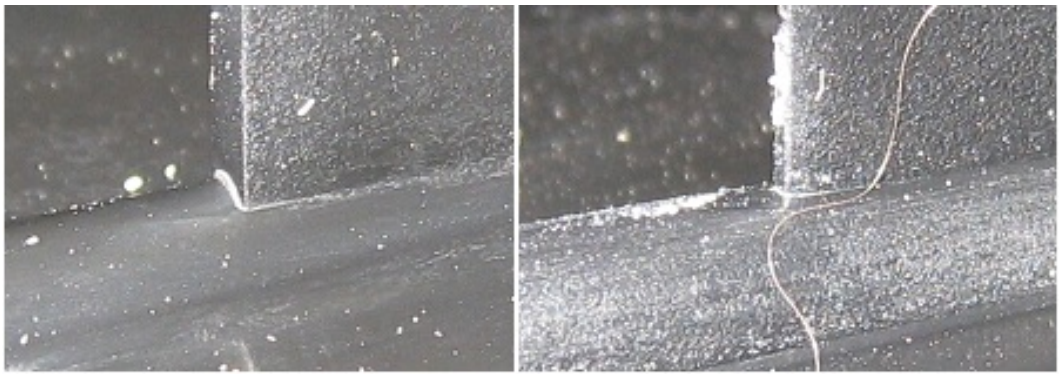

Figure 4.31: Left: Rib 3 of a 1.0 bar (15 psi) tested manifold cover showing a crack starting to propagate underneath the webbing. Right: Rib 7 of a 1.0 bar (15 psi) tested manifold cover possibly showing the beginnings of a crack. Both manifold covers were tested with new containment units.

At 0.7 bar (10 psi), nine manifold covers were tested with new containment units, and ten manifold covers were tested with old containment units. No indications of cracks or stress were observed on any of these manifold covers pressure tested at 0.7 bar.

In conclusion, only one crack was seen at Rib 3 on the 1.0 bar (15 psi) tested modules with another possibly starting at Rib 7 of a different cover in the same 1.0 bar (15 psi)

lot. No cracks or indications of stress were observed on any ribs for any of the 0.7 bar (10 psi) tested modules.

4.3.3 Summary of Internal Cracking of Manifold Cover in Various Pressure Testing Conditions

In order to determine acceptable pressure testing conditions, five sets of manifold covers were subjected to various pressure testing conditions. These were then examined for internal cracks.

Manifold covers under the following conditions were examined: sixteen with 1.4 bar (20 psi) old containment unit, nine with 1.0 bar (15 psi) new containment unit, nine with 0.7 bar (10 psi) new containment unit, ten with 0.7 bar (10 psi) old containment unit, and ten new from the box.

In the 1.4 bar (20 psi) tested manifold covers, ten of sixteen had cracks along the rib while seven of sixteen had cracks forming between the webbing and the rib. None of these cracks had yet progressed all the way through the manifold cover sidewall.

In all the manifold covers tested at less than 1.4 bar (20 psi), no cracks were found along the rib at all. One of nine 1.0 bar (15 psi) tested manifold covers had a possible crack initiation at the web-rib interface of Rib 3 and another at Rib 7, while none of the others had any cracks at all.

Table 4.4 provides a summary of the results.

4.3.4 Study of Stress Marks on Web-Rib Interface

When the web-rib interface for ribs 3, 5, and 7 is examined on a manifold cover, a white line can be seen which resembles a stress mark on the surface of the plastic. A polarized light source and viewer were used to determine which marks are stress marks and which are reflections off the small fillet at the interface. Polarized light is used to

	Crack along rib	Crack under webbing
1.4 bar old containment (16)	10	7
1.0 bar new containment (9)	0	1 Rib 3, 1 Rib 7
0.7 bar new containment (9)	0	0
0.7 bar old containment (10)	0	0
New (10)	0	0

Table 4.4: Number of manifold covers in each set exhibiting cracks at the specified locations on Rib 3. The number in parenthesis is the number of covers in that sample set.

illuminate the location of interest. The light reflects off the surfaces of the PVC keeping its original polarization. The portion of the fillet radius corresponding to the angle of the camera appears bright in a photograph of the interface. This is similar to how, in a sunset photograph over water, a portion of each wave reflects the sun to the viewer.

When a polarizer is applied to the lens of the camera at an orientation 90 degrees offset from the incident light, the reflected portion of the light is removed from the photograph. This can be seen in photographs of a new, non-pressure-tested manifold cover at Rib 3 as shown in Fig. 4.32.

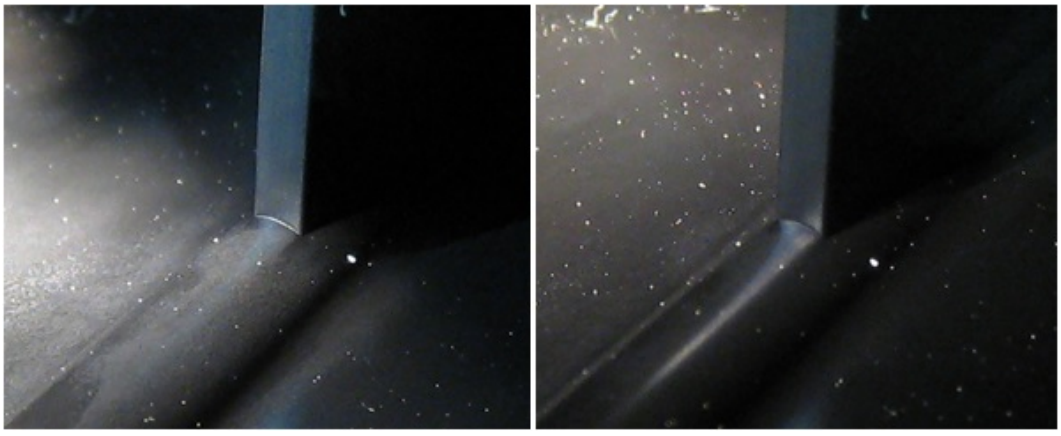

Figure 4.32: New manifold cover at Rib 3. Left: without polarizer on camera lens. Right: with polarizer on camera lens.

A stress mark on the surface of the plastic disrupts the smoothness of the surface and causes it to not reflect the light directly but instead serves as a diffuser and reflects the light without specific polarization. Thus if a stress mark is present instead of only a reflection, the orientation of the polarizer on the camera lens will not be able to eliminate the light as it was for the reflection. This can be seen in photographs of a 1.0 bar (15 psi) tested manifold cover at Rib 3 in Fig. 4.33.

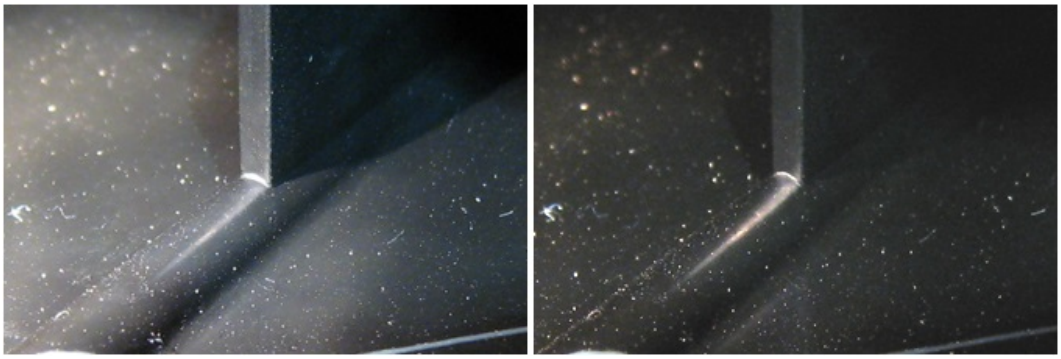

Figure 4.33: 1.0 bar (15 psi) new containment manifold cover at Rib 3. Left: without polarizer on camera lens. Right: with polarizer on camera lens.

To ensure the polarizer was not hiding some inherent polarization caused by cracking, this method was used to look at known cracks on 1.4 bar (20 psi) tested manifold covers at Rib 3. This method eliminated much of the background reflections while brightly illuminating the crack as shown in Fig. 4.34 thus indicating it would work to identify cracks.

Several manifold covers from mini-modules, modules constructed with shortened extrusions for the purpose of pressure testing for this study, were examined at Rib 3, 5, and 7 to see if stress marks are present. Nine manifold covers tested at 1.0 bar (15 psi) with new containment units, nine covers tested at 0.7 bar (10 psi) with new containment units, and ten covers tested at 0.7 bar (10 psi) with old containment units

Figure 4.34: Crack at Rib 3 in 1.4 bar (20 psi) tested with old containment manifold cover. Left: without polarizer on camera lens. Right: with polarizer on camera lens.

were examined.

At Rib 3, three out of ten 0.7 bar (10 psi) old containment manifold covers, two out of nine 0.7 bar (10 psi) new containment manifold covers, and two out of nine 1.0 bar (15 psi) new containment manifold covers were found to have a stress mark.

At Rib 5, five of ten 0.7 bar (10 psi) old containment manifold covers, three of nine 0.7 bar (10 psi) new containment manifold covers, and two of nine 1.0 bar (15 psi) new containment manifold covers were found to have a stress mark.

At Rib 7, eight of ten 0.7 bar (10 psi) old containment manifold covers, five out of nine 0.7 bar (10 psi) new containment manifold covers, and one of nine 1.0 bar (15 psi) new containment manifold covers were found to have a stress mark.

Ten new, non-pressure tested manifold covers were examined. One had a mark at Rib 3. None had a mark at Rib 5. Six had a mark at Rib 7.

A summary of these results can be seen in Table 4.5.

In conclusion, all three sample sets seem to be very similar at Rib 3 while the 0.7 bar (10 psi) old containment does appear to have more marks at Ribs 5 and 7. It appears

	Rib 3	Rib 5	Rib 7
1.4 bar old containment (16)	7*	n/a	n/a
1.0 bar new containment (9)	2**	2	1
0.7 bar new containment (9)	2	3	5
0.7 bar old containment (10)	3	5	8
New (10)	1	0	6

Table 4.5: Number of manifold covers exhibiting stress marks at each rib. The number of samples in a set is given in parentheses. *The 16 manifold covers pressure tested at 1.4 bar included 7 with stress marks, 7 with cracks, and two with neither stress marks nor cracks. **The 9 manifold covers pressure tested at 1.0 bar included 2 with stress marks, 1 with a small crack, and 6 with neither stress marks nor cracks.

that pressure testing the modules at 1.0 bar (15 psi) would not induce more stress marks than testing them at 0.7 bar (10 psi) with old containment.

It should be noted that none of the stress marks observed on any of the manifold covers tested at less than 1.4 bar (20 psi) exhibit any depth to them. By comparing the stress marks in Figs. 4.33 and 4.34 above, it can be seen that the stress mark on the cracked manifold cover extends slightly up the web rib interface while the stress mark on the uncracked manifold cover appears to be a surface phenomenon. Thus it is unlikely these stress marks would contribute to manifold cover cracking. Additionally, the manifold cover was redesigned to remove the ejection pin ribs and webbing, thus eliminating the concern for stress concentration and cracking along those features.

4.4 Summary of PVC Studies and Resulting Detector Design Changes

In Section 4.1, the tensile strength of a new manifold cover, molded from Geon M3800 PVC, was measured in several locations and found to be 80-90% that of the vendor's published value. A propensity to fail at Rib 3 was observed although the strength was similar to other locations not on the rib. One strength measurement near where cracks

had been observed on Rib 3 was nearly 20% lower than the other rib samples and could indicate a weak spot.

Section 4.2 looked at the performance of snout samples with a stress concentration from a corner with a small fillet radius. Increasing the fillet radius did seem to slightly improve the time until failure. But changing the PVC from Geon M3800 to the stronger Geon M3500 PVC greatly increased the time until failure. Additionally, it was observed that lower stress levels exponentially increased the time until failure in the stress concentration test.

Finally, Section 4.3 studied crack initiation in the manifold covers caused by pressure testing the manifold covers during module assembly. It was observed that reducing the pressure during the pressure test and improving the containment units used in the test appeared to eliminate cracks on the manifold cover.

In order to mitigate the risk of manifold cover cracking in the Far Detector, several changes were put into place in the design and construction of the modules.

The manifold cover and snout were redesigned to minimize stress concentrators by removing ejector pin ribs and webs which support the fiber raceways and increasing fillet radii as discussed in Section 4.2.4. Additionally, the PVC used to mold the manifold covers and snouts was changed to the stronger, tougher Geon M3500 instead of Geon M3800 as discussed in Section 4.2.4.

The pressure test containment units were stiffened as described in Section 4.3.2, and the pressure applied during the pressure test was lowered from 1.4 bar to 0.7 bar based on results from Section 4.3.2.

Chapter 5

Conclusion and Discussion

5.1 Review of the Thesis

Chapter 2 discusses adhesive strength studies using aged adhesives and PVC surface treatments for the acrylic and epoxy adhesives used in construction of the NOνA detector. It was found that both adhesive varieties tended to have steady or increased strength when aged, and that surface treatment appears beneficial for both epoxy and acrylic adhesive types.

In Chapter 3, interaction studies were performed on all construction materials for interaction with the pseudocumene scintillator to ensure all materials that might degrade the scintillator could be eliminated from the detector or isolated from the scintillator.

Finally, Chapter 4 contains studies on injection molded PVC manifold covers examining the strength of the PVC in various locations and orientations on the manifold cover, making stress tolerance comparisons between PVC varieties, and studying cracking in manifold covers which have been pressure tested at various pressure levels and with varying containment units.

5.2 Contributions to Literature

Interaction studies for liquid scintillators and especially pseudocumene is novel and not abundant in the literature. One paper from the University of Minnesota deals with the interaction of scintillator and optical fiber but only addresses the effect of the pseudocumene on the fiber[21]. Since the detector being built out of PVCs and various adhesives is a new concept, studies of the effects of materials on pseudocumene has not been approached before and are a novel contribution to the body of literature. The studies reported in this thesis will be valuable for future experiments with pseudocumene scintillator.

Studies addressing stress concentrations in PVC do not appear in literature. Failure of the PVC could be attributed to a combination of creep and stress concentration. While the work presented in this thesis is early, it was useful toward guiding the redesign of the NOνA detector manifold cover and snouts.

5.3 Recommendations for Future Work

In Chapter 2, a guideline was used which suggested that adhesive aging effects are approximately accelerated by a factor of two for each 10°C increase in temperature. This guideline was suggested by a vendor and could not be validated elsewhere but is alluded to in several sources. The guideline could be related to the general guideline that chemical reactions are often accelerated by a factor of approximately two for each 10°C increase in temperature.

As more structures are incorporating various adhesives as construction materials, it would be valuable to learn how adhesives tend to age and how to study aging accelerated by heating. Future studies could compare adhesives aged at various elevated temperatures to those aged at room temperature for several representative adhesives such as the

epoxy and acrylic used in Chapter 2. The study could be expanded to include various substrate categories such as PVC and aluminum.

Further investigation could be done in pseudocumene liquid scintillator interaction studies. The studies described in Chapter 3 of this thesis provided qualitative analysis of scintillator interaction with various materials. While all these results were desired for the design and construction of the NOνA detectors, it would be valuable to learn more precisely how much various materials interact with the liquid scintillator instead of merely studying if the materials do interact.

Further studies could control the surface area of the materials being studied and obtain quantitative measurements of interaction.

Longer term interaction studies would be valuable to see if interacting components leech out over long periods of time. To facilitate consistent readings of samples, a fixture to precisely reorient each sample should be developed instead of merely using visual alignment. This will allow non-continuous comparisons to be compared with greater confidence.

Additionally, the phototube apparatus could be placed in a temperature stable environment to minimize variations caused by sensitivity to daily room temperature cycles. An additional study could be performed on interactions of materials and scintillator at elevated temperatures which could perhaps speed interactions or simulate possible detector environments.

Much more work could be done in the areas of PVC stress concentration and creep. This work could build off the techniques shown in this thesis but with improved statistics. Fillet stress concentration factors could be measured for thermoplastics with a time component to the concentration factor.

5.4 Finito

In conclusion, this thesis describes several distinct and disparate yet important prongs of research which are unified by the NOνA experiment whose detectors were recently completed and began taking data which will help us better understand the fundamental nature of our universe.

References

[1] Feldman, Gary et al. NOνA Technical Design Report, 2007. URL `http://www-nova.fnal.gov/nova_cd2_review/tdr_oct_23/tdr.htm`.

[2] Friedland, Alexander and Shoemaker, Ian M. Searching for Novel Neutrino Interactions at NOvA and Beyond in Light of Large theta_13. *arXiv preprint arXiv:1207.6642*, 2012.

[3] Blennow, Mattias and Schwetz, Thomas. Identifying the neutrino mass ordering with INO and NOvA. *Journal of High Energy Physics*, vol. 2012(8):pp. 1–17, 2012.

[4] Michael, D.G., Adamson, P., Alexopoulos, T., et al. The magnetized steel and scintillator calorimeters of the MINOS experiment. *Nuclear Instruments and Methods in Physics Research Section A: Accelerators, Spectrometers, Detectors and Associated Equipment*, vol. 596(2):pp. 190–228, 2008.

[5] Chase, Thomas. NOvA Module Design, 2007. NOVA-docdb-2715-v3, October 2007.

[6] Crawford, Russell J. *Plastics engineering*. Butterworth-Heinemann, 1998.

[7] Nitti, Benjamin M. *Adhesive Seals in PVC to PVC Bonds For NOνA Modules*. Master's thesis, University of Minnesota, 2008.

[8] 3M Scotch-Weld Epoxy Adhesives. DP190 Translucent and Gray Technical Data, 2010. URL http://multimedia.3m.com/mws/media/667100/3m-scotch-weld-epoxy-adhesive-dp190-translucent-gray.PDF.

[9] Devcon. Plastic Welder Technical Data Sheet, 2011. URL http://www.devcon.com/prodfiles/pdfs/fam_tds_182.pdf.

[10] D3807, ASTM Standard. Standard Test Method for Strength Properties of Adhesives in Cleavage Peel by Tension Loading (Engineering Plastics-to-Engineering Plastics), 1998 (2012). URL www.astm.org.

[11] 6922(1987), ISO Standard. Adhesives Determination of Tensile Strength of Butt Joints, 1987. URL www.iso.org.

[12] D3528, ASTM Standard. Standard Test Method for Strength Properties of Double Lap Shear Adhesive Joints by Tension Loading, 1996 (2008). URL www.astm.org.

[13] Renkert Oil. Fermi Scintillator. *Material Safety Data Sheet*, 2012. NOVA-docdb-7270-v2, November 2012.

[14] JabberWok. File:Compton-scattering.svg — Wikipedia, The Free Encyclopedia, 2012. [Online; accessed 21-December-2012], URL http://en.wikipedia.org/wiki/File:Compton-scattering.svg.

[15] Pla-Dalmau, Anna, Bross, Alan D., and Rykalin, Victor V. Extruding plastic scintillator at Fermilab. In *Nuclear Science Symposium Conference Record, 2003 IEEE*, vol. 1, pp. 102–104. IEEE, 2003.

[16] D638, ASTM Standard. Standard Test Method for Tensile Properties of Plastics, 2010. URL www.astm.org.

[17] PolyOne. Geon Vinyl Rigid Molding M3800. URL http://catalog.ides.com/Datasheet.aspx?I=55275&FMT=PDF&U=1&CULTURE=en-US&E=146887.

[18] Software, Yet Another Webcam, Version 0.3.3 (2010-02-28). URL http://www.yawcam.com/.

[19] PolyOne. Geon Vinyl Rigid Molding M3500. URL http://catalog.ides.com/Datasheet.aspx?I=55275&FMT=PDF&U=1&CULTURE=en-US&E=35027.

[20] Nowak, Jarek. Tests at UMN, 2010. NOVA-docdb-5158-v1, August 2010.

[21] Strait, M., Cronin-Hennessy, D., and Arms, K. Interaction rate of polystyrene fiber optics with pseudocumene-based liquid scintillator. *Nuclear Instruments and Methods in Physics Research Section A: Accelerators, Spectrometers, Detectors and Associated Equipment*, vol. 615(1):pp. 33–36, 2010.

Appendix A

Measured Values For Tensile Adhesive Strength

All tensile tests had an adhesive test area of 25 mm by 3.2 mm (1" by 0.125") or 8.1×10^{-5} m^2 (0.125 in^2).

A.1 Acrylic Adhesive Tensile Strength Measurements

Acrylic Tensile Test, Unaged, No Surface Treatment		
Sample:	Maximum load (lb)	Ultimate Tensile Strength (MPa)
1	400.4	22.08
2	398.0	21.95
3	342.0	18.86
4	359.4	19.82
5	348.3	19.21
6	371.4	20.49
7	339.2	18.71
8	270.5	14.92
9	308.8	17.03
10	274.9	15.16
Mean		18.82
Standard Error of the Mean		0.79

Acrylic Tensile Test, Unaged, Sanded PVC Surface		
Sample:	Maximum load (lb)	Ultimate Tensile Strength (MPa)
1	396.4	21.86
2	417.2	23.01
3	382.5	21.09
4	398.1	21.96
5	434.1	23.94
6	435.0	23.99
Mean		22.64
Standard Error of the Mean		0.49

Acrylic Tensile Test, Unaged, Corona Discharge Treated PVC Surface		
Sample:	Maximum load (lb)	Ultimate Tensile Strength (MPa)
1	431.3	23.79
2	379.2	20.92
3	343.6	18.95
4	364.2	20.09
5	382.8	21.11
6	410.1	22.62
Mean		21.25
Standard Error of the Mean		0.71

Acrylic Tensile Test, 9 months in Oil, Sanded PVC Surface		
Sample:	Maximum load (lb)	Ultimate Tensile Strength (MPa)
1	408.2	22.50
2	397.7	21.94
3	385.9	21.27
4	467.5	25.78
5	356.2	19.64
Mean		22.23
Standard Error of the Mean		1.01

Acrylic Tensile Test, 9 months in Air, Corona Discharge Treated		
Sample:	Maximum load (lb)	Ultimate Tensile Strength (MPa)
1	512.5	28.23
2	502.0	27.65
3	558.8	30.78
4	437.3	24.08
5	456.4	25.13
Mean		27.17
Standard Error of the Mean		1.19

Acrylic Tensile Test, 9 months in Oil, Corona Discharge Treated		
Sample:	Maximum load (lb)	Ultimate Tensile Strength (MPa)
1	370.5	20.40
2	393.0	21.64
3	476.5	26.24
4	473.1	26.07
5	334.4	18.42
Mean		22.56
Standard Error of the Mean		1.56

A.2 Epoxy Adhesive Tensile Strength Measurements

Epoxy Tensile Test, Unaged, Sanded PVC Surface		
Sample:	Maximum load (lb)	Ultimate Tensile Strength (MPa)
1	223.0	12.30
2	178.8	9.86
3	200.6	11.06
4	171.8	9.47
Mean		10.68
Standard Error of the Mean		0.64

Epoxy Tensile Test, Unaged, Corona Discharge Treated PVC Surface		
Sample:	Maximum load (lb)	Ultimate Tensile Strength (MPa)
1	221.9	12.24
2	169.3	9.34
3	185.5	10.23
4	245.6	13.55
Mean		11.34
Standard Error of the Mean		0.95

Epoxy Tensile Test, 9 months in Air, Sanded PVC Surface		
Sample:	Maximum load (lb)	Ultimate Tensile Strength (MPa)
1	130.2	7.18
2	222.9	12.29
3	208.5	11.50
4	167.9	9.26
Mean		10.06
Standard Error of the Mean		1.15

Epoxy Tensile Test, 9 months in Oil, Corona Discharge Treated		
Sample:	Maximum load (lb)	Ultimate Tensile Strength (MPa)
1	196.2	10.82
2	226.4	12.49
3	288.7	15.92
4	183.4	10.12
5	236.7	13.06
Mean		12.48
Standard Error of the Mean		1.01

Epoxy Tensile Test, 9 months in Air, Corona Discharge Treated		
Sample:	Maximum load (lb)	Ultimate Tensile Strength (MPa)
1	224.8	12.40
2	237.7	13.11
3	267.0	14.72
4	216.4	11.94
5	195.3	10.77
Mean		12.59
Standard Error of the Mean		0.66

Epoxy Tensile Test, 18 months in Air, Sanded PVC Surface		
Sample:	Maximum load (lb)	Ultimate Tensile Strength (MPa)
1	261.3	14.41
2	164.8	9.09
3	226.5	12.49
4	147.4	8.13
5	223.2	12.31
Mean		11.29
Standard Error of the Mean		1.16

Epoxy Tensile Test, 18 months in Oil, Sanded PVC Surface		
Sample:	Maximum load (lb)	Ultimate Tensile Strength (MPa)
1	200.2	11.04
2	119.2	6.57
3	154.7	8.53
4	170.6	9.41
Mean		8.89
Standard Error of the Mean		0.93

Appendix B

Interaction Study Results

Results plots of interaction testing for various materials of interest for the construction of the NOνA detectors as described in Chapter 3.

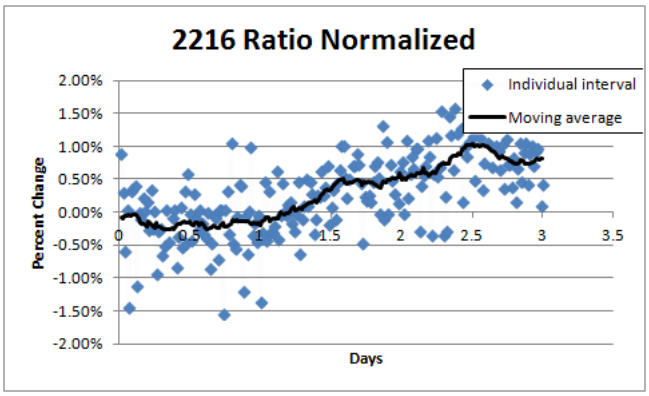

Figure B.1: This plot shows the interaction results of the 2216 Epoxy used as the inner adhesive in the detectors' dual-adhesive joint design. The lack of decrease of the ratio over 3 days indicates no interaction.

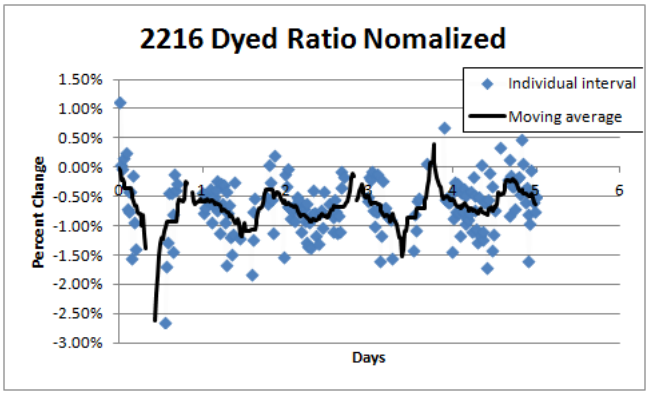

Figure B.2: This plot shows the interaction results of the Dyed 2216 Epoxy, a potential substitute for the 2216 Epoxy used as the inner adhesive in the detectors' dual-adhesive joint design. The lack of decrease of the ratio over 5 days indicates no interaction.

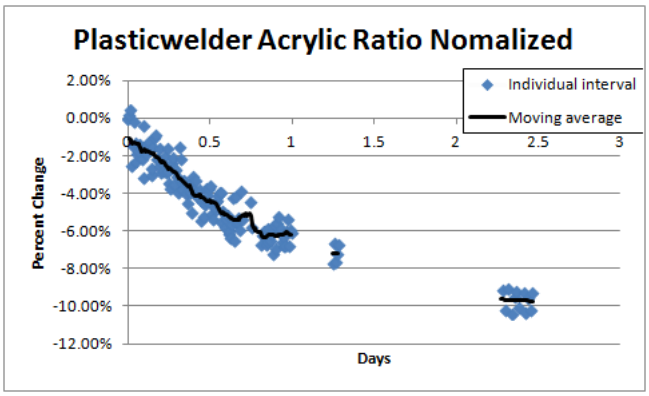

Figure B.3: This plot shows the interaction results of the Plastic Welder Acrylic used as the outer adhesive in the detectors' dual-adhesive joint design. The significant, steady decrease over 3 days indicates strong interaction of the acrylic with the scintillator.

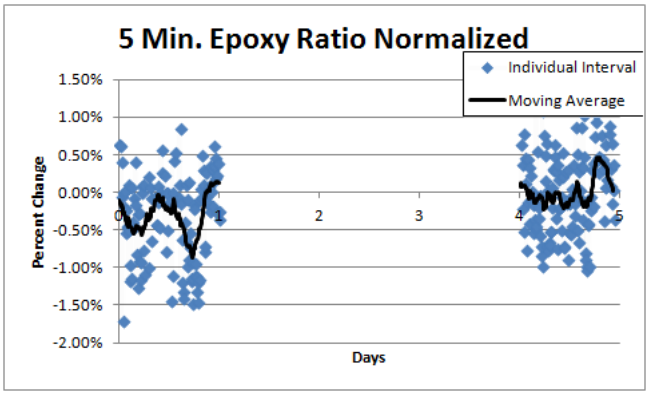

Figure B.4: This plot shows the interaction results of the 5 Minute Epoxy used in assembly of the detector modules. The lack of decrease of the ratio over 5 days indicates no interaction.

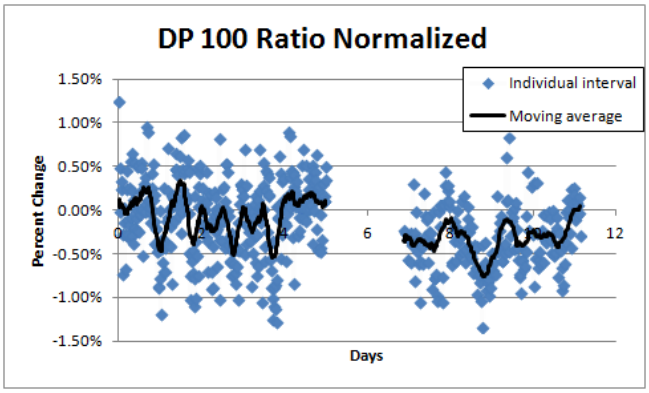

Figure B.5: This plot shows the interaction results of the DP 100 Epoxy; the steadiness of the ratio over 11 days indicates no interaction.

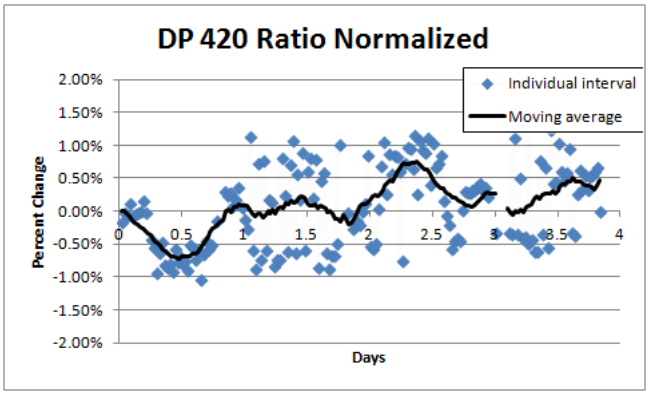

Figure B.6: This plot shows the interaction results of the DP 420 Epoxy; the steadiness of the ratio over 4 days indicates no interaction.

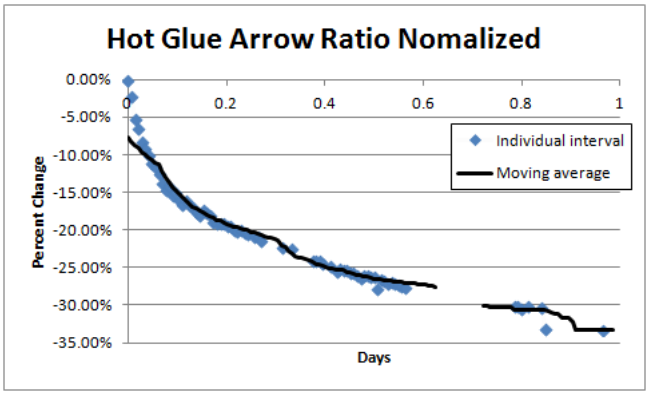

Figure B.7: This plot shows the interaction results of Arrow Hot Glue used as the outer adhesive in the detectors' dual-adhesive joint design. The significant, steady decrease over 1 day indicates strong interaction of the hot glue with the scintillator.

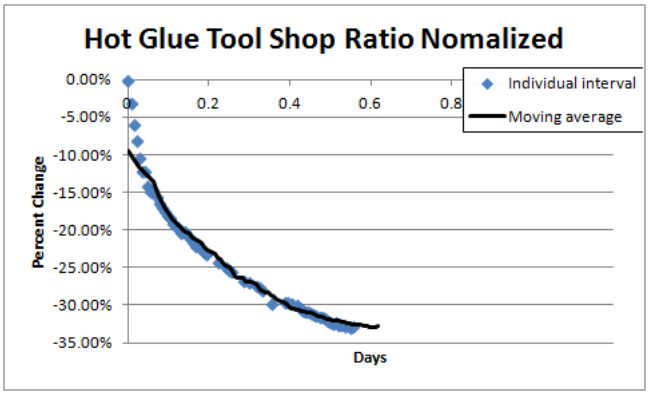

Figure B.8: This plot shows the interaction results of Tool Shop Hot Glue used as the outer adhesive in the detectors' dual-adhesive joint design. The significant, steady decrease over less than a day indicates strong interaction of the hot glue with the scintillator.

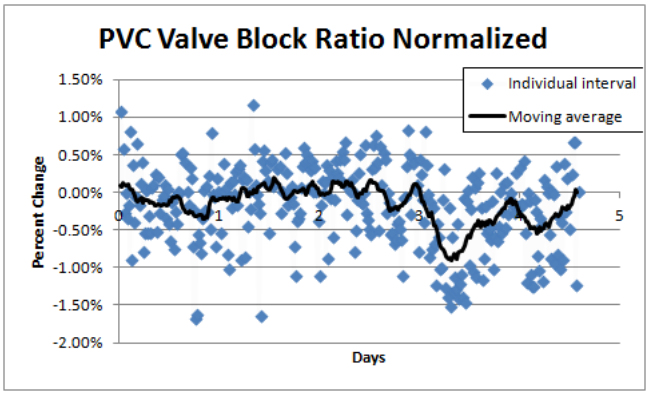

Figure B.9: This plot shows the interaction results of PVC for use in mounting the drain valve. The steadiness of the ratio over 4.5 days indicates no interaction.

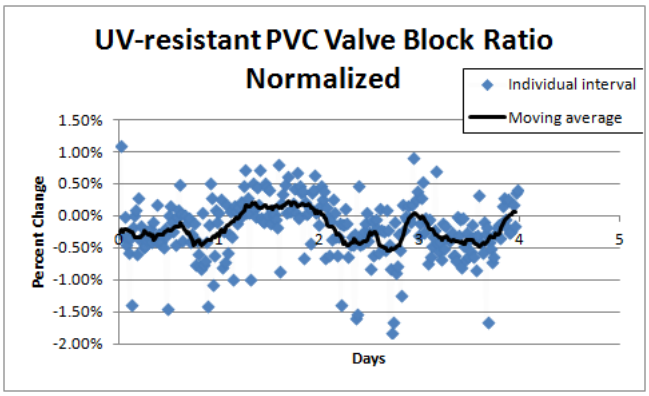

Figure B.10: This plot shows the interaction results of UV-resistant PVC for use in mounting the drain valve. The steadiness of the ratio over 4 days indicates no interaction.

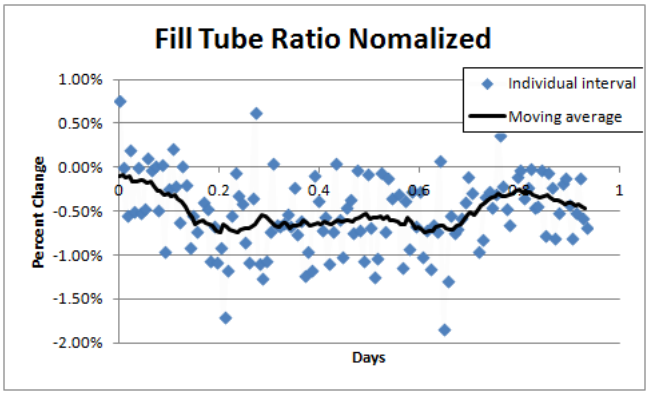

Figure B.11: This plot shows the interaction results of the PVC tube used to fill the detector modules. The steadiness of the ratio over 1 day indicates no interaction.

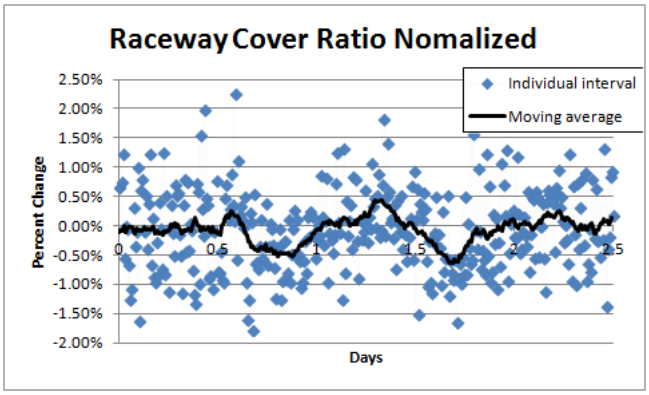

Figure B.12: This plot shows the interaction results of the PVC sheeting used to cover the raceway to keep the fibers in place. The steadiness of the ratio over 2.5 days indicates no interaction.

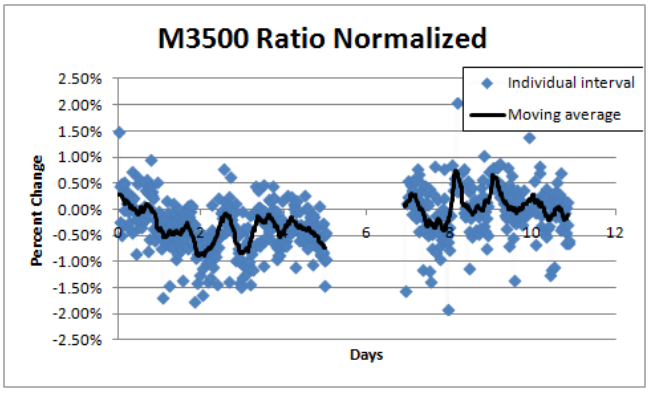

Figure B.13: This plot shows the interaction results of the Geon M3500 PVC used in the new manifold covers and snouts. The steadiness of the ratio over 11 days indicates no interaction.

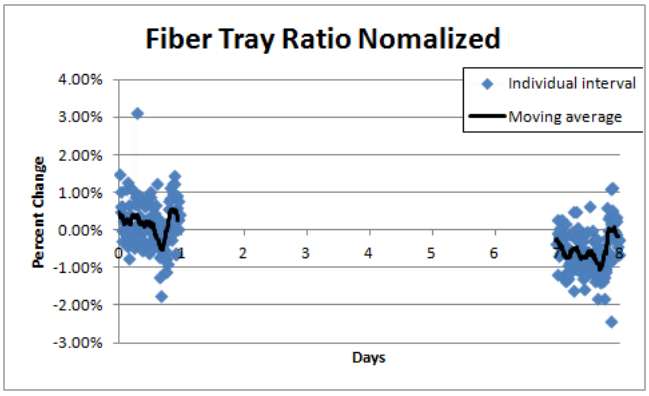

Figure B.14: This plot shows the interaction results of the extruded PVC raceways used to guide the fibers from the cells to the optical connector. The steadiness of the ratio over 8 days indicates no interaction.

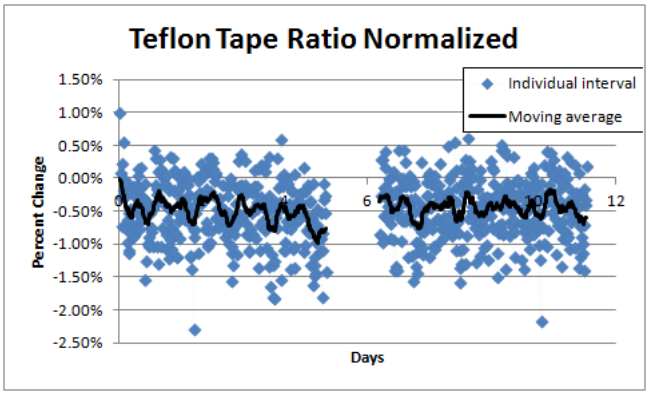

Figure B.15: This plot shows the interaction results of PTFE tape used to plumb the drain valve. The steadiness of the ratio over 11 days indicates no interaction.

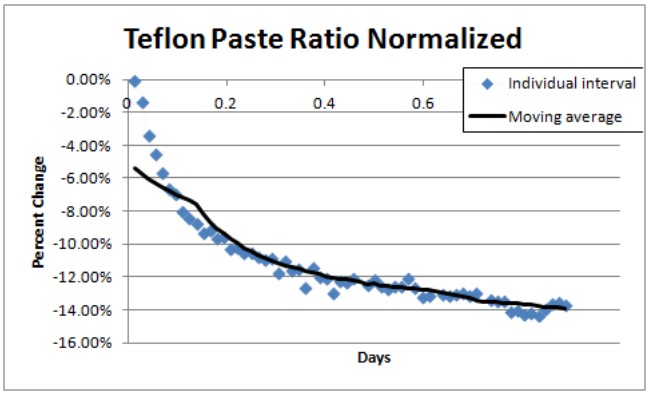

Figure B.16: This plot shows the interaction results of PTFE tape used to plumb the drain valve. The significant, steady decrease over a day indicates strong interaction of the PTFE paste with the scintillator.

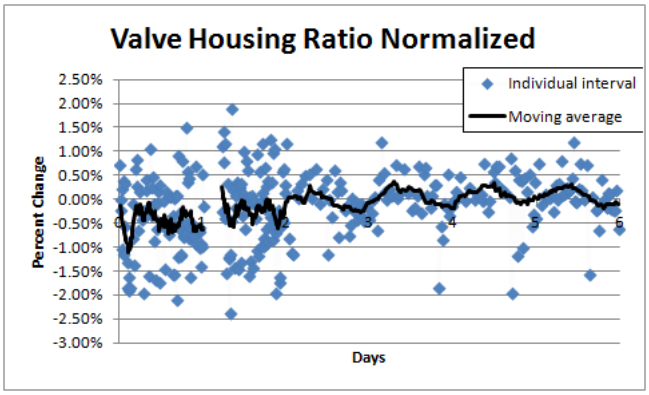

Figure B.17: This plot shows the interaction results of the housing of the globe valve used as the module drain valve. The steadiness of the ratio over 6 days indicates no interaction.

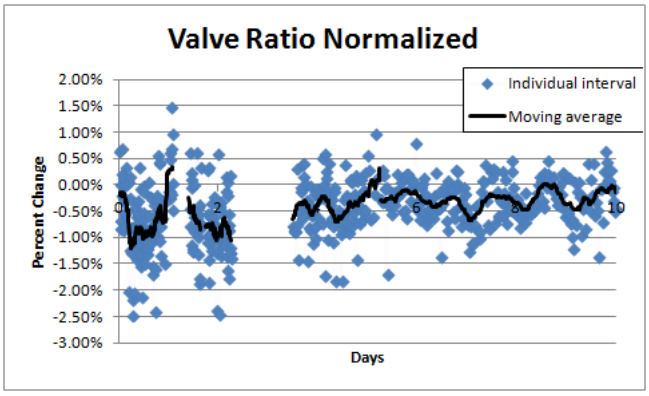

Figure B.18: This plot shows the interaction results of the globe valve used as the module drain valve. The steadiness of the ratio over 10 days indicates no interaction.